NEUROSCIENCE

WWC1 mutation drives dopamine dysregulation and synaptic imbalance in Tourette's syndrome

Junkai Lv[1,2]†, Shiqi Liang[1,2]†, Pengwei Qin[1,2]†, Xinlu Liu[1,2], Xiangyu Ge[1,2], Yiqing Guo[1,2], Shili Xia[1,2], Wei Jing[1,2,3], Youming Lu[1,2,4]*, Tongmei Zhang[1,2,5]*, Hao Li[1,2]*

Tourette's syndrome (TS) is a major neurodevelopmental disorder characterized by childhood-onset motor and vocal tics. A W88C mutation in *WWC1* gene is a notable risk factor for TS, but the underlying molecular mechanisms remain unclear due to the lack of suitable animal models. Here, we generate a mutant mouse line with human W88C mutation (W88C^Mut mice), which exhibits behavioral deficits similar to those observed in patients with TS, including repetitive motor behaviors and sensorimotor gating abnormalities. The W88C mutation leads to the degradation of kidney and brain (KIBRA) protein via a proteasomal pathway, evokes dopamine release in the dorsal striatum, and disrupts synaptic function through the dysregulation of Hippo pathway. Neuron-specific overexpression of wild-type *WWC1* rescues synaptic and behavioral phenotypes in W88C^Mut mice. Together, this study not only provides a valuable mouse model for studying TS but also offers fresh insights into the molecular and synaptic mechanisms underlying neurodevelopmental abnormalities in TS.

INTRODUCTION

Tourette's syndrome (TS), a neurodevelopmental disorder marked by childhood-onset motor and vocal tics, manifests as a complex array of involuntary movements and vocalizations, often prefaced by premonitory urges (*1*, *2*). Affecting about 0.3 to 0.9% of the global population, TS shows a higher incidence in males, with a male-to-female ratio of ~4:1 (*3*, *4*). Individuals with TS frequently experience comorbid conditions, including obsessive-compulsive disorder (OCD), attention deficit hyperactivity disorder (ADHD), learning and memory challenges, and mood disorders (*5*). Adolescents with TS particularly struggle to develop adequate social and educational skills and to maintain psychological health (*6*). Despite the notable impact of TS, research into its underlying mechanisms and targeted treatments has been limited, with an increasing trend in diagnoses (*7*, *8*).

The origins of TS are not entirely understood but are largely linked to genetic factors, evidenced by a high familial heritability rate (*9*). A recent whole-exome sequencing study involving 511 TS samples identified the *WWC1* gene as a key risk factor, with its W88C mutation being particularly notable. This mutation, occurred in the third exon of *WWC1*, changed the nucleotide sequence from G to T, resulting in the substitution of tryptophan (W) with cysteine (C) at the 88th amino acid position, and was considered deleterious (*10*), indicating its probable role in the pathogenesis of TS.

The protein encoded by *WWC1*, known as Kibra, is widely and abundantly expressed in brain (Allen Brain Atlas: Mouse Brain). Previous research has highlighted its notable role in neural development (*11*, *12*), synaptic plasticity (*13*, *14*), and estrogen receptor activation (*15*). Despite its apparent relevance to TS-related abnormalities, direct evidence linking Kibra to TS has been elusive. Thus, constructing an animal model to investigate the role of Kibra in TS and its viability as a disease model is crucial.

Our earlier research conclusively showed that the W88C mutation, located in the WW domain of Kibra crucial for protein-protein interactions, leaded to diminished protein stability and reduced binding affinity with other proteins (*16*). In the present study, we revealed that the W88C mutation notably affects Kibra's functionality within the central nervous system. Mice with this mutation exhibited repetitive motor behaviors, sensorimotor gating deficits, and dopamine signaling abnormalities, mirroring symptoms seen in human patients with TS. This highlights the importance of the W88C mutant mouse model for investigating TS pathogenesis.

In combining behavioral assessments and molecular analyses, our study seeks to illuminate the consequences of the W88C mutation in the *WWC1* gene, particularly its impact on dopamine signaling and neurodevelopmental processes. Our multifaceted approach places this research at the cutting edge of neuroscience, addressing pivotal questions in TS pathology and potentially charting valuable directions for therapeutic interventions.

RESULTS

Enhanced repetitive motor behaviors and sensorimotor gating deficits in W88C^homo mice

In our quest to model TS in a murine system, we focused on the W88C mutation in the *WWC1* gene. This mutation, identified in patients with TS (*10*), is known to influence critical neural functions (*16*). Our goal is to validate whether W88C homozygous (W88C^homo) mice can effectively replicate the core symptoms of TS, thereby providing a meaningful model for studying the disorder's pathophysiology. Using CRISPR-Cas9 gene-editing technology, we successfully introduced the W88C mutation into the murine *WWC1* gene, creating W88C heterozygous (W88C^hete) and W88C homozygous (W88C^homo) mice (fig. S1A). These mice undergo extensive characterization to confirm the presence of mutation and to ensure the absence of notable

[1]Innovation Center for Brain Medical Sciences of the Ministry of Education, Huazhong University of Science and Technology, Wuhan 430030, China. [2]Department of Pathophysiology, School of Basic Medicine and Tongji Medical College, Huazhong University of Science and Technology, Wuhan 430030, China. [3]Department of Anatomy, School of Basic Medicine, Tongji Medical College, Huazhong University of Science and Technology, Wuhan 430030, China. [4]Department of Physiology, School of Basic Medicine and Tongji Medical College, Huazhong University of Science and Technology, Wuhan 4030030, China. [5]Department of Histology and embryology, School of Basic Medicine, Tongji Medical College, Huazhong University of Science and Technology, Wuhan 430030, China.
*Corresponding author. Email: lihaochn@hust.edu.cn (H.L.); zhtm@hust.edu.cn (T.Z.); lym@hust.edu.cn (Y.L.)
†These authors contributed equally to this work.

developmental disabilities or structural brain anomalies, as evidenced by their comparable body and brain tissue weights to wild-type (WT) controls (fig. S1, B to D). Additionally, Nissl staining of serial coronal sections from anterior to posterior regions of the brain further substantiated the absence of any discernible structural differences between the two genotypes (fig. S1E).

To evaluate the behavioral phenotype of W88C^homo mice, we initially focused on extended home-cage monitoring to capture spontaneous repetitive motor behaviors. Given the notable behavioral differences between mice and humans, we defined repetitive motor behaviors in mice as stereotyped motor activities that significantly exceed normal levels, analogous to the tics observed in TS. During this observation period, W88C^homo mice exhibited significantly enhanced repetitive motor movements, including hyperactivity (accelerated head swinging), sniffing, digging, and grooming, which resonate with the motor tics characteristic of TS (Fig. 1A). These behaviors are inherently spontaneous and consistently manifest in familiar, stress-minimized environments, reinforcing their relevance to the core symptoms of TS (1). Subsequently, the open-field test, designed to simulate a novel environment, provided further insights. In this setup, W88C^homo mice displayed reduced overall locomotion (Fig. 1B), with a notable increase in repetitive motor behaviors during periods of immobility (Fig. 1B). In patients with TS, involuntary movements compete with normal behavior, and reinforcing competitive actions can alleviate tic symptoms (17). Similarly, mutant mice exhibit repetitive motor behaviors that interfere with normal exploratory activities, reducing their travel distance. This pattern suggested that the repetitive motor movements were not merely stress responses but intrinsic to the effect of mutation on behavior. This observation has been recapitulated in the W88C^homo mice, where repetitive motor movements are pronounced, independent of stress-inducing stimuli, pointing to the inherent influence of the W88C mutation on behavior patterns. Our analyses extended to evaluating the latency to action initiation within novel environments, an aspect critical in the assessment of TS. When subjected to a variety of behavioral assays, including the open field (fig. S2A), elevated plus maze (fig. S2B), and Y-maze tests (fig. S4C), W88C^homo mice demonstrated a consistent pattern of prolonged latencies before engaging in exploratory actions (Fig. 1C). The pole climbing test provided further confirmation of this phenomenon. W88C^homo mice exhibited extended times in both the initiation and execution of the climbing task (Fig. 1D). The repetitive motor behaviors of the W88C^homo mice can be observed on video (movies S1 and S2).

As the method used to generate W88C mutant mice is not limited to the central nervous system, there is a notable risk of confounding variables due to peripheral expression. To address potential nonspecific and unexpected effects in the periphery, we conducted a comprehensive histological validation of the skin in WT and W88C^homo mice. We examined skin samples from dorsal, facial, and cervical regions using hematoxylin and eosin (H&E) staining, toluidine blue staining, and CD45 immunohistochemistry (fig. S3A). Quantitative analysis revealed no significant differences in the thickness of epidermal, corium, and subcutaneous tissue layers between WT and W88C^homo mice across all examined skin regions (fig. S3B). Furthermore, we assessed mast cell density in the corium, a key indicator of skin inflammation and irritation. No significant differences were observed between genotypes in any of the analyzed skin areas (fig. S3C). To evaluate potential immune cell infiltration, we quantified the percentage of CD45^+ area in the corium, which showed

comparable levels between WT and W88C^homo mice (fig. S3D). These results collectively demonstrate that the skin structure and immune cell composition in W88C^homo mice are indistinguishable from those of WT littermates. Thus, we can conclude that the repetitive motor behaviors exhibited by W88C^homo mice is not attributable to compromised skin health or peripheral sensory abnormalities, suggesting that the observed phenotype likely originates from central nervous system dysfunction rather than peripheral factors.

Sensorimotor gating capabilities, assessed via the prepulse inhibition (PPI) test, were significantly compromised in W88C^homo mice, unlike in WT or W88C^hete mice (Fig. 1E). Notably, these PPI deficits did not extend to generalized acoustic startle responses, as demonstrated by consistent startle amplitudes across all genotypes when PPI was not in effect (fig. S2F). The specificity of the PPI impairment reinforces its potential relevance to the sensorimotor gating disturbances characteristically observed in TS (18), while the normal startle response indicates that the W88C mutation does not disrupt basic auditory processing or reflexive motor pathways.

To ensure that our observations were specific to the W88C mutation, we tested a range of behaviors of potential relevance to other domains of neuropsychiatric pathology. These tests, including the open field, elevated plus maze, sucrose preference test, and tail suspending test, showed no significant differences in anxiety-like behaviors or depressive symptoms between W88C^homo mice and WT controls (fig. S2, A to D). Performance in the rotarod test, which assessed motor skill and coordination, did not show a significant difference between the W88C homozygous mice and their WT littermates (fig. S2E). This suggests that the W88C mutation does not directly impair the mice's motor coordination capabilities. Cognitive functions were assessed through various tests including the Morris water maze, Y-maze, fear conditioning (FC), novel object recognition, and three-chamber social test. W88C^homo mice did not show significant differences in learning and memory capabilities compared to WT or heterozygous mice (fig. S4, A to G), although a reduction in exploration time in social settings was noted (fig. S4, F and G). This comprehensive approach highlights that the W88C mutation specifically induces repetitive motor behaviors and sensorimotor gating deficits without broadly affecting other aspects of behavior and cognition, further validating the W88C^homo mouse model as a relevant tool for studying TS pathophysiology.

The W88C mutation was identified in a human TS family, with human carriers being heterozygous (10). However, in the behavioral tests mentioned above, we did not observe TS-like behavior in W88C^hete mice. Therefore, we believe that the TS-like behavior in W88C^hete mice is milder and less detectable. Because repetitive motor behaviors in some mouse models are associated with inducing/destabilizing manipulations (6), we applied stress stimulation to amplify the TS-like behavior in W88C^hete mice. We administered a 2-s foot shock to the mice, followed by 20 min of open-field testing, analyzing various indicators (fig. S5, A and B). We found that WT mice showed the greatest increase in movement distance over time, while their repetitive motor behaviors increased the least. In contrast, W88C^hete mice exhibited significant differences compared to WT mice in all indicators except for digging, where there was still a trend toward a difference (fig. S5B). Meanwhile, W88C^homo mice had the smallest increase in movement distance and the highest increase in repetitive motor behaviors over time (fig. S5, A and B). Therefore, through stress stimulation, we could amplify the TS-like behavior in W88C^hete mice, making it observable in experimental
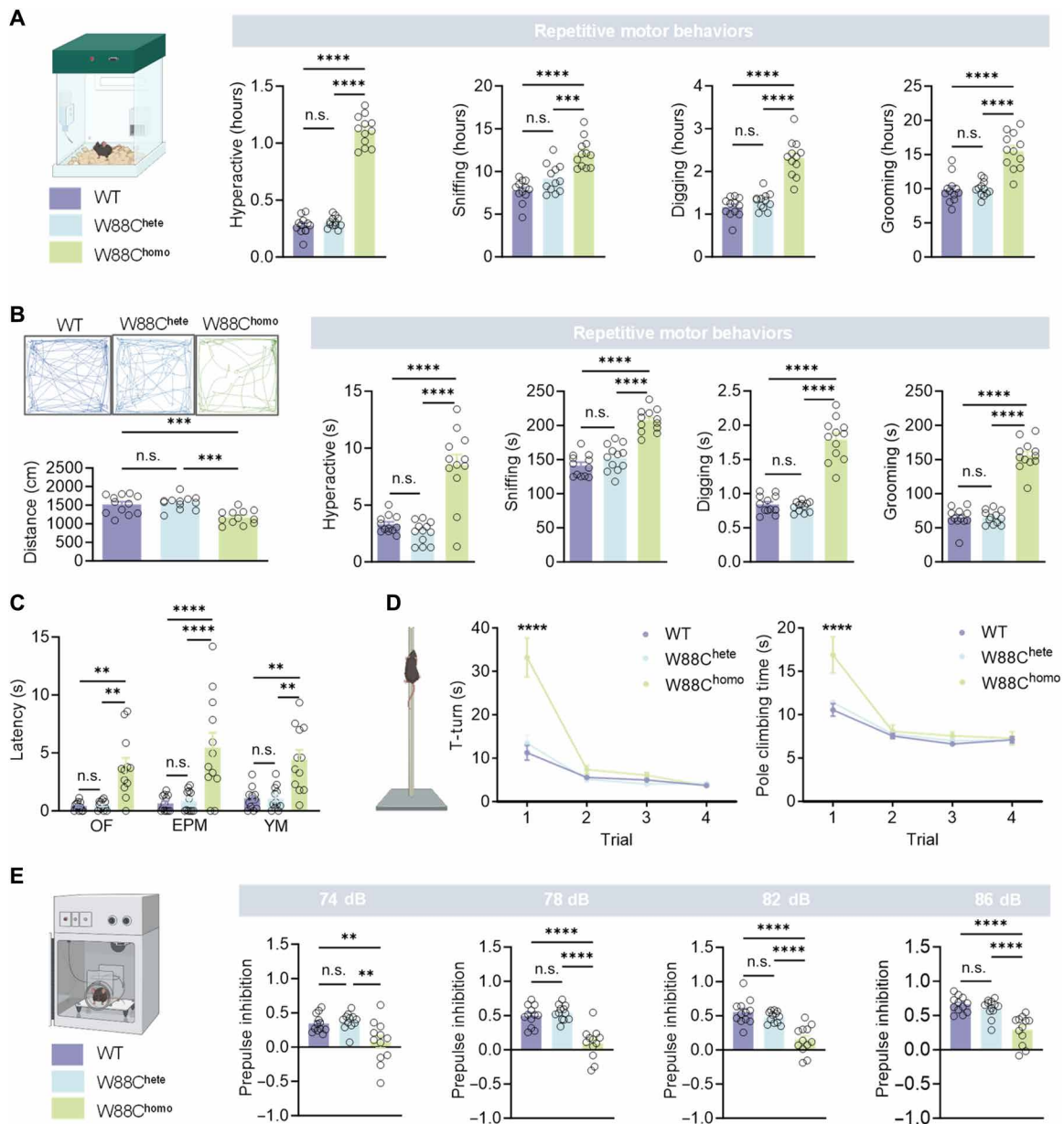
Fig. 1. Repetitive motor behaviors and impaired sensorimotor gating in W88C^{homo} male mice. (**A**) Duration of spontaneous behaviors in home cage, with repetitive motor behaviors (hyperactive, sniffing, digging, and grooming) predominating in W88C homozygotes. $n = 12$ per genotype; n.s. (not significant), $P > 0.05$; ***$P < 0.001$; ****$P < 0.0001$, one-way analysis of variance (ANOVA) with Tukey's multiple comparisons test. (**B**) Left: Open-field trajectories with quantification of total distance, showing hypoactivity in W88C homozygous mice. $n = 12$ per genotype; ***$P < 0.001$, one-way ANOVA with Dunnett's multiple comparisons test. Right: Open-field behaviors, highlighting increased repetitive motor activity (hyperactive, sniffing, digging, and grooming) during immobility in W88C^{homo} mice. $n = 12$ per genotype; n.s., $P > 0.05$; ****$P < 0.0001$, one-way ANOVA with Dunnett's multiple comparisons test. (**C**) Extended latency to action initiation in W88C^{homo} mice across behavioral assays. The graph depicts the latency periods before movement initiation in W88C^{homo} mice compared to that in wild-type (WT) controls across various behavioral assays. The open-field test (OF), elevated plus maze (EPM), and Y-maze (YM) assessments demonstrate significantly prolonged latencies for the W88C^{homo} mice before commencing exploratory behavior, indicative of delayed reactivity in unfamiliar environments. $n = 12$ per genotype; **$P < 0.01$; ****$P < 0.0001$, one-way ANOVA with Tukey's multiple comparisons test. (**D**) Pole test times for turning (T-turn) and descending (pole climbing), illustrating delayed responses in initial trials for W88C homozygotes. $n = 12$ per genotype; ****$P < 0.0001$, two-way ANOVA with Tukey's multiple comparisons test. (**E**) The prepulse inhibition (PPI) of the acoustic startle reflex response across decibel levels, with W88C homozygotes showing sensorimotor gating impairments. PPI values are expressed as a proportion. $n = 12$ per genotype; n.s., $P > 0.05$; **$P < 0.01$; ****$P < 0.0001$, one-way ANOVA with Tukey's multiple comparisons test. Data are all presented as means ± SEM.

settings. Under stress conditions, W88C[hete] mice still exhibited milder TS-like behavior compared to W88C[homo] mice. This finding clarifies the link between the W88C mutation and TS, enhancing the phenotypic similarity between W88C mutant mice and human patients with TS.

Given the discovery of TS-like features in male W88C[homo] mice, we pondered whether female W88C[homo] mice would manifest similar anomalies. In evaluating the behavioral phenotype of W88C[homo] female mice, home-cage monitoring revealed that female W88C[homo] mice exhibited mild enhanced repetitive motor movements, including hyperactivity, sniffing, and grooming (fig. S6A). Subsequently, the open-field test revealed that female W88C[homo] mice displayed slight reduced overall locomotion (fig. S6B), with a mild increase in repetitive motor behaviors during periods of immobility (fig. S6B). When subjected to a variety of behavioral assays, including the open field, elevated plus maze, and Y-maze tests, female W88C[homo] mice did not show prolonged latencies (fig. S6C). In the pole climbing test, female W88C[homo] mice exhibited slight prolongation in both the initiation and execution of the climbing task (fig. S6D). Sensorimotor gating capabilities, assessed via the PPI test, were slightly compromised in female W88C[homo] mice (fig. S6E). Additionally, female W88C[homo] mice did not exhibit reduced exploration time in the three-chamber social test (fig. S6, F and G). These results suggest that female W88C[homo] mice exhibit TS-like behavioral characteristics, albeit to a lesser extent compared to male mice.

The comprehensive approach of precise genetic engineering and detailed behavioral profiling in W88C[Mut] mice offers valuable insights into TS. This model replicates key symptoms such as motor tics and sensorimotor gating deficits, facilitating further exploration of the genetic and neurobiological mechanisms of TS.

W88C-induced Kibra protein degradation via ubiquitin-proteasome pathway

In probing the influence W88C mutation on *WWC1* gene expression and consequent effects on Kibra protein, we sought to elucidate the molecular basis of TS. Acknowledging the pivotal role of Kibra in neural development and synaptic modulation (*11–14*), our research aimed to decipher how this genetic alteration manifested at a molecular level. Initially, quantitative real-time polymerase chain reaction (PCR) was used to measure *WWC1* mRNA levels across WT, W88C[hete], and W88C[homo] mice. Despite the presence of mutation, we observed no significant variations in mRNA expression relative to WT controls (Fig. 2A), indicating that the effects of W88C mutation on Kibra might be enacted posttranscriptionally. Subsequent Western blot analysis of brain tissue extracted from W88C mutant mice revealed a notable decrease in Kibra protein levels, a quarter reduction in W88C[hete] and more than half in W88C[homo] mice compared to that in WT controls (Fig. 2B). This marked decline underscores the extensive neural impact of W88C mutation.

Given the disparity between stable mRNA levels and reduced protein expression, we deduced that the W88C mutation predominantly accelerated the degradation of Kibra rather than diminishing its synthesis, pointing to posttranslational mechanisms, especially within protein degradation pathways, as the culprits for reduced Kibra levels in W88C mutants. To further unravel these mechanisms, we conducted experiments with human embryonic kidney (HEK) 293T cells transfected with plasmids from both *Mus musculus* and *Homo sapiens*, encoding either the *WWC1*[WT]–green fluorescent protein (GFP) or *WWC1*[W88C]-GFP variants. Dissecting the degradation

pathway involved treatments with synthesis inhibitor [cycloheximide (CHX)], a lysosome inhibitor [bafilomycin A1 (Baf)], and a proteasome inhibitor (MG132). Post–CHX treatment, Western blot analysis demonstrated that the degradation rate of W88C-Kibra was significantly higher than that of WT-Kibra in cells expressing plasmids from both species (Fig. 2, C and D, and fig. S7, A and B). Notably, this degradation was significantly attenuated by the proteasome inhibitor MG132, indicating a proteasome-dependent degradation pathway, whereas the lysosome inhibitor Baf did not exhibit a similar protective effect (Fig. 2, E and F, and fig. S7, C and D). To eliminate the possibility of other potential factors contributing to the degradation of W88C-Kibra, we treated cells transfected with *WWC1*[W88C-GFP] solely with MG132. We observed that the expression level of W88C-Kibra gradually increased over time, eventually surpassing the expression level of untreated WT-Kibra (Fig. 2, G and F). This demonstrates that the increased proteasomal degradation is the reason for the decreased protein expression level of W88C-Kibra. Further investigation into the role of ubiquitination was conducted through immunoprecipitation (IP) assays. These assays revealed a significant increase in ubiquitination levels of Kibra in *WWC1*[W88C]-GFP–expressing cells, particularly following MG132 treatment (Fig. 2, H and I). This pattern was consistent in human-origin *WWC1* plasmids (fig. S7, G and H), bolstering the hypothesis that W88C mutation escalated ubiquitin-proteasome-mediated Kibra degradation.

In summary, these findings compellingly suggest that the W88C mutation primarily induces increased degradation of Kibra through the ubiquitin-proteasome pathway, rather than lysosomal degradation. This molecular insight into the impact of the W88C mutation on Kibra stability offers a deeper understanding of protein degradation processes, potentially involved in the pathophysiology of disorders linked to *WWC1* gene mutations.

Enhanced dopamine signaling in the dorsal striatum of W88C[homo] mice

In our investigation into the neurobiological mechanisms of TS, we focused on the striatal region, a critical component of the corticostriatal-thalamic-cortical (CSTC) circuit (*19*). This circuit, implicated in the pathology of TS, encompasses key neural hubs for motor control, executive functions, and procedural learning (*20–22*). Dysregulation of dopamine signaling within the striatum, a key feature in the CSTC circuit, has been hypothesized as a notable factor in TS pathogenesis (*23*, *24*).

Dopamine in the striatum primarily regulates functions such as motor control, motivation, and reward through interactions with D1R and D2R (*25*). In TS, a contributing factor is the lack of inhibition in the striatum, and therapeutic strategies targeting the D2R pathway to enhance striatal inhibition have proven effective (*26*). To quantify dopamine activity in the striatum, we injected a hSyn promoter–driven DA2h dopamine fluorescent sensor, which is engineered on the basis of the D2R receptor, into the dorsal striatum of both WT and W88C[homo] mice (Fig. 3, A and B). Optical fibers were then implanted at standardized coordinates in the dorsal striatum, ensuring consistent placement across all experimental groups (fig. S8A). Fiber photometry recordings revealed a significantly higher frequency of dopamine release in the dorsal striatum of W88C[homo] mice compared to that of WT (Fig. 3, C and D), aligning with dopamine dysregulation hypotheses in TS (*23*, *24*). Building on this discovery, we explored the therapeutic potential of haloperidol, a D2
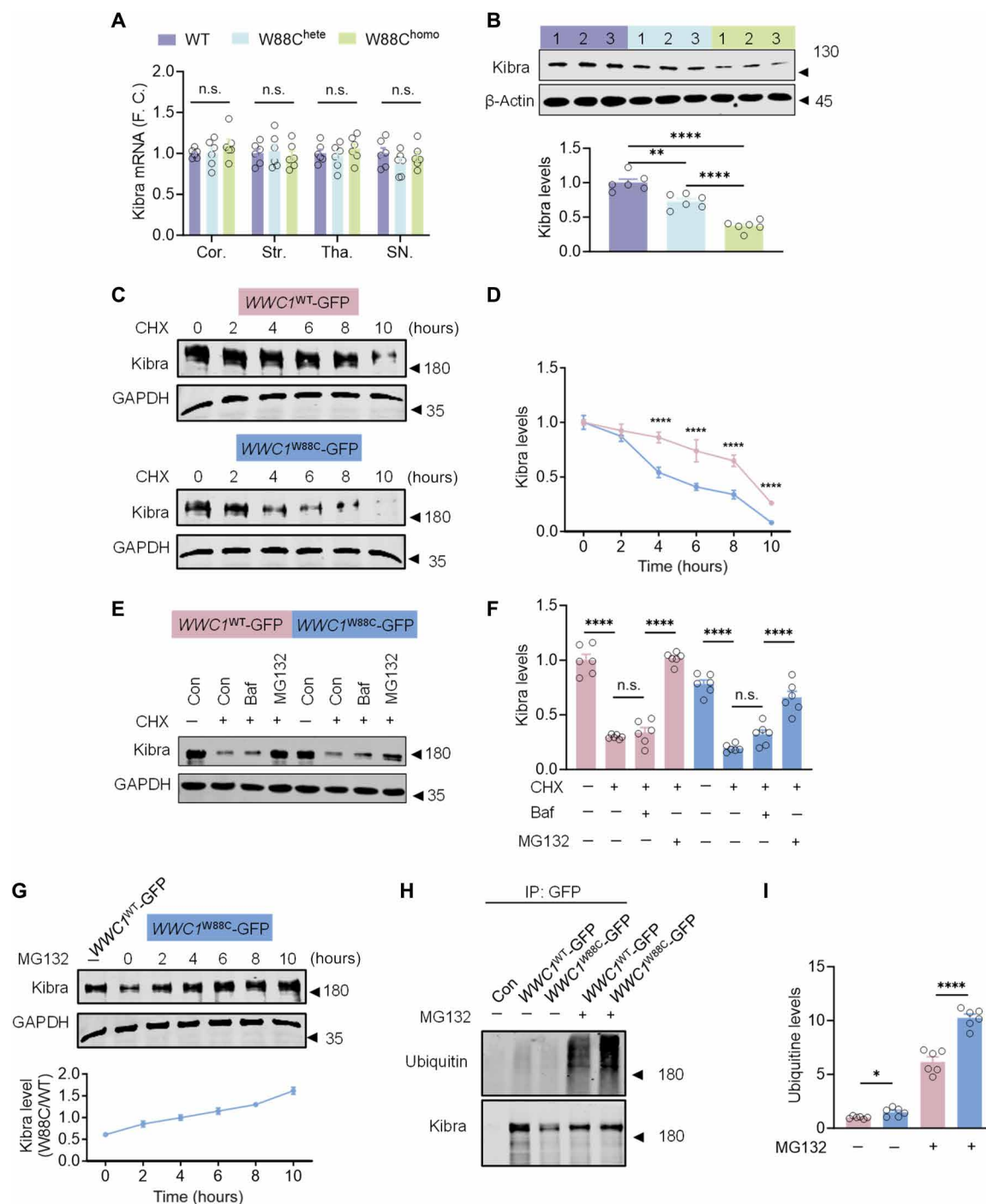
Fig. 2. Kibra ubiquitination and proteasomal degradation in W88C mutant mice. (**A**) No significant changes in Kibra mRNA levels in cortex (Cor.), striatum (Str.), thalamus (Tha.), and substantia nigra (SN.) of WT, W88C[hete], and W88C[homo] mice. $n = 6$ per group; n.s., $P > 0.05$; one-way ANOVA with Tukey's multiple comparisons test. F.C., fold change. (**B**) Western blots and quantitative analysis showing Kibra protein levels in the brain are markedly reduced in W88C[hete] and W88C[homo] mice compared to those in WT, indicating enhanced protein degradation. $n = 6$ per group; **$P < 0.01$ and ****$P < 0.0001$, unpaired t test. (**C** and **D**) Cell-based assay with *WWC1*[WT]-GFP– and *WWC1*[W88C]-GFP–transfected HEK293 cells treated with cycloheximide (CHX) shows *WWC1*[W88C] promoted Kibra degradation. GAPDH, glyceraldehyde-3-phosphate dehydrogenase. (**E** and **F**) Cell-based assay with *WWC1*[WT]-GFP– and *WWC1*[W88C]-GFP–transfected HEK293 cells treated with CHX shows Kibra degradation, which is prevented by proteasome inhibitor MG132, not by lysosome inhibitor bafilomycin A1 (Baf). $n = 6$ per group; n.s., $P > 0.05$; ****$P < 0.0001$, two-way ANOVA with Tukey's multiple comparisons test. (**G**) Cell-based assay with *WWC1*[WT]-GFP– and *WWC1*[W88C]-GFP–transfected HEK293 cells treated with MG132 prevented Kibra degradation. (**H**) Immunoprecipitation (IP) assay revealing increased ubiquitination of Kibra in *WWC1*[W88C]-GFP–expressing cells upon MG132 treatment. (**I**) Densitometry confirms enhanced ubiquitination of Kibra in presence of MG132. $n = 6$ per group; *$P < 0.05$ and ****$P < 0.0001$, one-way ANOVA with Tukey's multiple comparisons test. All protein expression levels are normalized to the values of the internal control protein. Data are all presented as means ± SEM.
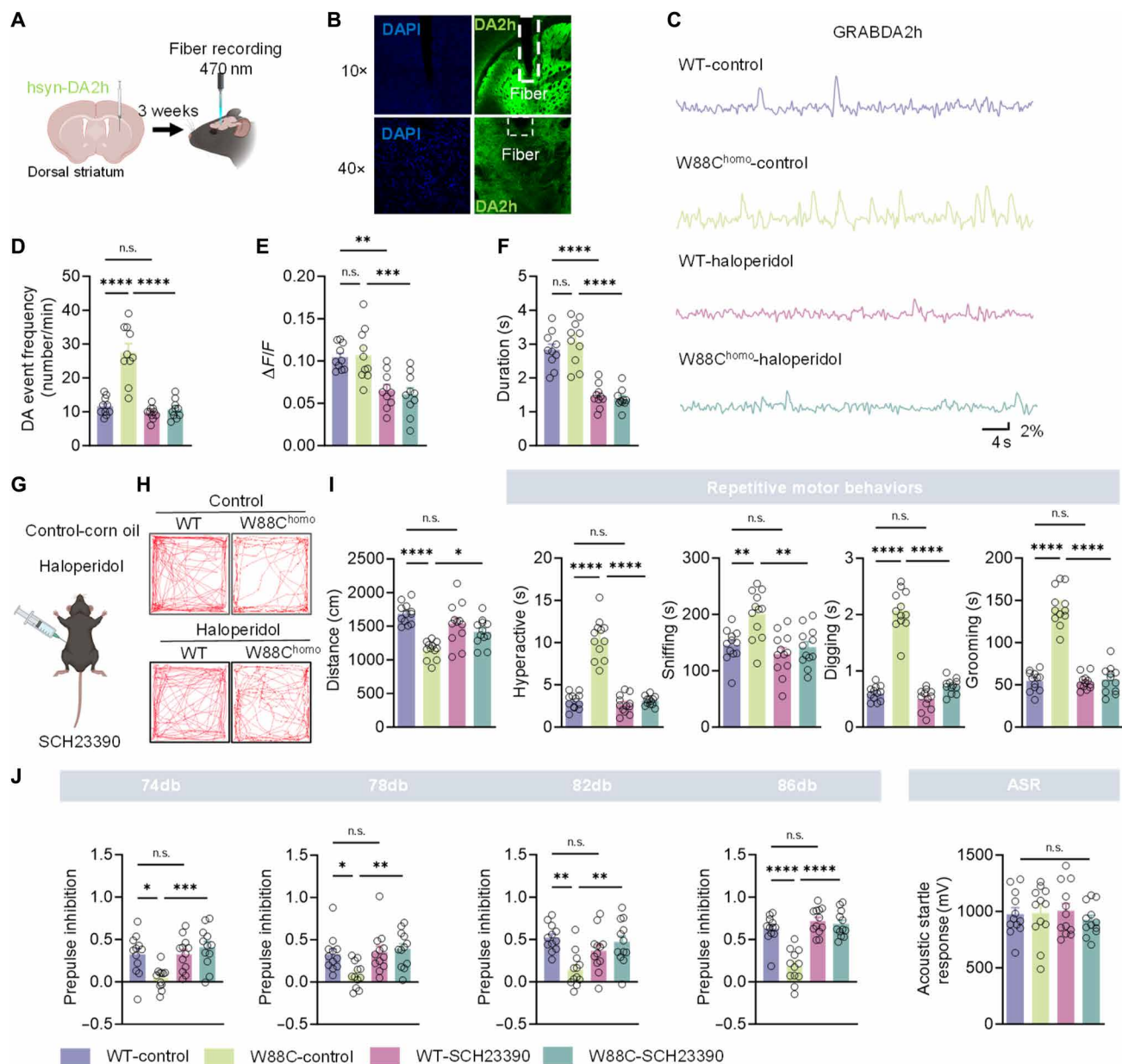
Fig. 3. W88C^homo male mice exhibit dopamine dysregulation and respond to haloperidol and SCH23390 treatment. (**A**) Schematic depicting viral-mediated hSyn-DA2h delivery and subsequent fiber photometry setup in the dorsal striatum for in vivo dopamine monitoring and dynamic dopamine signal recording. (**B**) Microscopic validation of DA2h expression and fiber placement in the dorsal striatum. (**C** and **D**) In vivo fiber photometry traces (C) and quantitative analysis (D) demonstrate significantly elevated dopamine events in W88C^homo mice compared to those in controls, which are effectively normalized following haloperidol treatment. $n = 10$ per group. (**E** and **F**) Detailed quantification of the peak $\Delta F/F$ (change in fluorescence relative to baseline fluorescence) (E) and the duration of dopamine events (F) shows a significant decrease in both parameters following haloperidol treatment. $n = 10$ per group. (**G**) Schematic illustration of the corn oil (vehicle), haloperidol and SCH23390 administration protocol in WT and W88C^homo mice. (**H**) Open-field test trajectories and aggregate distance traveled, showing behavioral attenuation with haloperidol treatment. $n = 12$ per group. (**I**) Comprehensive quantification of repetitive motor behaviors showing significant reduction following haloperidol treatment. $n = 12$ per group. (**J**) Assessment of sensorimotor gating through PPI showing restoration of PPI in SCH23390-treated W88C^homo mice. $n = 12$ per group; n.s., $*P < 0.05$; $**P < 0.01$; $***P < 0.001$; $****P < 0.0001$, two-way ANOVA with Tukey's test or two-way RM ANOVA for PPI. Data are all presented as means $\pm$ SEM.

receptor antagonist known for its efficacy in TS (*27*). Administering haloperidol [0.1 mg/kg, intraperitoneal (ip)] dissolved in corn oil to the W88C^homo mice led to a significant normalization of the previously observed dopaminergic anomalies (Fig. 3, C and D). While haloperidol treatment reduced the amplitude of DA (dopamine) peaks, there were no significant differences in DA peak amplitude

between WT and W88C^homo mice without haloperidol treatment (Fig. 3, E and F). This pharmacological intervention not only reduced the elevated dopamine levels but also brought a notable improvement in the repetitive motor behaviors, as evidenced by open-field test (Fig. 3, G to I). However, haloperidol did not rescue the PPI abnormalities in W88C^homo mice (fig. S9A), whereas SCH23390

(15 μg/kg, ip), a D1 receptor antagonist, effectively rescues the PPI deficits in W88C[homo] mice (Fig. 3J). This dual effect, rectifying both neurochemical and behavioral abnormalities, was specific to the W88C[homo] mice, as similar treatment in WT mice did not yield comparable changes (Fig. 3, G to J).

Our research suggests that TS-like behaviors in W88C[homo] mice are associated with abnormal dopamine release. Previous studies have indicated a positive correlation between repetitive motor behaviors and dopamine release (28, 29). Although some research studies suggest that PPI is also influenced by dopamine signaling (30–33), the regulatory mechanisms between sensorimotor gating deficits and dopamine remain unclear. Existing studies have demonstrated that the basal ganglia in mice exhibit corresponding dopamine signaling responses to auditory stimuli (34–36). Therefore, we aimed to analyze the dopamine signal patterns associated with different PPI responses by recording dopamine signal in conjunction with PPI testing in mice to strengthen the connection between dopamine abnormalities induced by WWC1 mutation and sensorimotor gating deficits.

Because the PPI deficits in W88C[homo] mice are primarily mediated by D1R, and existing studies have shown that auditory stimuli are converted into behavioral outcomes mainly through D1R in the dorsal striatum (37), we injected a hSyn promoter–driven dLight1.1 dopamine fluorescent sensor, which is engineered on the basis of the D1R receptor, into the dorsal striatum of W88C[homo] and WT mice (fig. S10, A and B). Optical fibers were then implanted at standardized coordinates in the dorsal striatum, ensuring consistent placement across all experimental groups (fig. S8A). This allowed us to record the dynamic changes in dopamine signals mediated by D1R during PPI testing. Recording dopamine signals after different prepulse stimuli revealed that W88C[homo] mice exhibit a distinct dopamine signal pattern compared to WT mice (Fig. 4, A and B). For each decibel of prepulse stimulus, the dLight1.1 response induced in W88C[homo] mice was greater than that in WT mice (Fig. 4E). Additionally, the dLight1.1 response after the acoustic startle response (ASR) stimulus was also greater in W88C[homo] mice than in WT mice (Fig. 4E). This difference was eliminated by administering the D1R antagonist SCH23390 (Fig. 4, C to E). The time for the dopamine signal to return to baseline did not differ between W88C[homo] and WT mice under various prepulse stimuli and ASR, whether SCH23390 was used or not (fig. S11A). These findings, combined with our previous pharmacological studies showing that D1R antagonists, but not D2R antagonists, can improve PPI deficits in W88C[homo] mice, suggest that abnormal dopamine signaling through D1R may play a critical role in the disrupted regulation of PPI responses in these mice. We observed enhanced dopamine signaling in the DLS during PPI tests, extending our understanding of PPI neural circuits. While previous studies have primarily emphasized the role of nucleus accumbens and dorsomedial striatum (38, 39), our data suggest that dopamine signaling in the DLS may also play an important role in PPI regulation. This view is supported by our pharmacological experiments: The altered dopamine dynamics in the DLS region closely correlate with the behavioral phenotype. Future studies could further validate these findings through region-specific interventions. This suggests patterns of dopamine dysregulation in W88C[homo] mice that may help frame models and generate testable hypotheses regarding sensorimotor gating deficits in patients with TS, potentially guiding the development of targeted therapies for different dopamine response patterns.

Our observations highlight the notable role of striatal dopamine signaling in TS-like symptoms. The effectiveness of haloperidol and SCH23390 in alleviating neurochemical imbalances and resultant behavioral symptoms in W88C[homo] mice underscores the involvement of dopaminergic dysregulation TS pathology. This insight not only aids our understanding of the disorder but also provides new directions for treatment strategies focused on modulating striatal dopamine dynamics.

Altered neuronal activation and synaptic dynamics in the striatal circuitry of W88C[homo] mice

The elevated dopamine levels detected in the dorsal striatum prompted us to investigate neuronal activation patterns within the cortico-striatal circuitry of W88C[homo] mice, using c-Fos as a marker for neuronal activity. Our analysis revealed an increased prevalence of c-Fos–positive neurons in the dorsal striatum and primary motor cortex (M1) in W88C[homo] mice relative to that in WT controls (Fig. 5, A and B, and fig. S12A). This hyperactivation within cortico-striatal pathways could be intricately linked to tic generation, consistent with the dopaminergic dysregulation hypothesis of TS. To delve deeper into the synaptic implications of these findings, we centered our investigations on medium spiny neurons (MSNs), the primary neuronal population in the striatum. Whole-cell patch-clamp recordings revealed augmented frequencies of both miniature and spontaneous excitatory postsynaptic currents (mEPSCs and sEPSCs) in MSNs of W88C[homo] mice, with no significant changes in amplitude (Fig. 5, C and D). These observations suggest an amplified presynaptic release of glutamate. In parallel, the analysis of inhibitory postsynaptic currents (both miniature and spontaneous, mIPSCs and sIPSCs) demonstrated a reduced frequency in W88C[homo] mice as opposed to their WT counterparts, without amplitude alterations (Fig. 5, E and F). This reduction in inhibitory input, coupled with enhanced excitatory synaptic activity, culminates in an elevated excitatory/inhibitory (E/I) synaptic ratio (Fig. 5, G and H), delineating a potential synaptic basis for the increased dopaminergic activity and heightened neuronal activation observed. To verify whether W88C[homo] mice exhibit TS characteristics in cortico-striatal connectivity, we conducted recordings of cortico-striatal synaptic circuitry in acute brain slices. We found that the field population spikes were significantly increased in W88C[homo] mice compared to those in the controls (Fig. 5I). These synaptic dynamics, characterized by an E/I imbalance, are reflective of the neuropathological signatures commonly associated with various neuropsychiatric disorders (40), including TS. The intricate interplay between enhanced dopaminergic release, cortico-striatal overactivation, and E/I synaptic disequilibrium provides a compelling synaptic narrative for the observed behavioral phenotypes in W88C[homo] mice.

Previous studies have indicated that Kibra, a postsynaptic density protein, is affected by the W88C mutation, which weakens its binding ability with Dendrin (16). Complete disruption of Kibra-Dendrin binding in the hippocampus leads to changes in postsynaptic density (PSD) components, reduced mEPSP amplitude, and impaired learning and memory (16, 41, 42). First, we extracted proteins from the hippocampal tissues of W88C[homo] and WT mice and found that the levels of Kibra were also significantly reduced in the hippocampus of W88C[homo] mice (fig. S13, A and B). Therefore, we extracted hippocampal PSD from W88C[homo] and WT mice and found no significant differences in the composition of postsynaptic and receptor components (fig. S13, C and D). Using cell filling, we assessed the dendritic spine density in the CA1 and DG regions of the hippocampus in both W88C[homo] and WT mice and found no significant
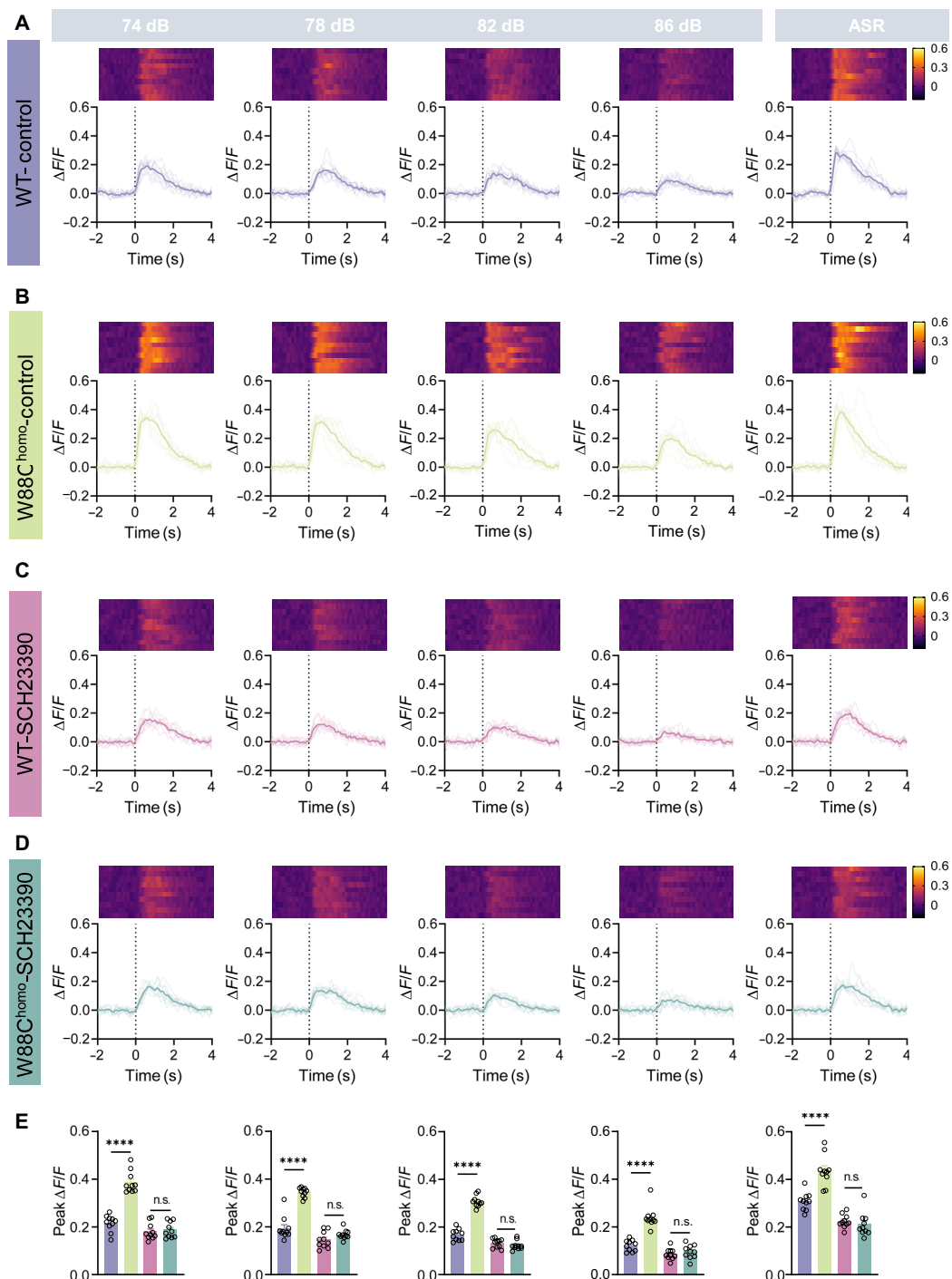
Fig. 4. The W88C^homo male mice showed an abnormal dopamine signaling response pattern to sound stimuli in the PPI and could be improved by SCH23390. (**A**) Fiber photometry data showing dopamine signaling response to prepulse stimuli (74, 78, 82, and 86 dB) and acoustic startle response (ASR) in WT control mice. The top panels display heatmaps of signal intensity over time, while the bottom panels show the average $\Delta F/F$ traces. $n = 10$ per group. (**B**) Dopamine signaling response in W88C^homo-control mice, indicating an abnormal pattern of signal transduction in response to sound stimuli compared to that in WT controls. The top panels display heatmaps of signal intensity, and the bottom panels show the average $\Delta F/F$ traces. $n = 10$ per group. (**C**) Dopamine signaling response in WT mice treated with SCH23390 (WT-SCH23390). The response patterns to sound stimuli and ASR are consistent with the control group, suggesting no significant alteration due to SCH23390 treatment. The top panels display heatmaps of signal intensity, and the bottom panels show the average $\Delta F/F$ traces. $n = 10$ per group. (**D**) Dopamine signaling response in W88C^homo mice treated with SCH23390 (W88C^homo-SCH23390). SCH23390 treatment normalizes the abnormal dopamine signaling response patterns observed in untreated W88C^homo mice, bringing them closer to the WT response patterns. The top panels display heatmaps of signal intensity, and the bottom panels show the average $\Delta F/F$ traces. $n = 10$ per group. (**E**) Quantification of the peak $\Delta F/F$ responses to prepulse stimuli (74, 78, 82, and 86 dB) and ASR, showing significant differences between W88C^homo and WT mice, and normalization of responses in W88C^homo mice treated with SCH23390. $n = 10$ per group; n.s., $P > 0.05$; ****$P < 0.0001$, two-way repeated measures ANOVA followed by Tukey's post hoc test for multiple comparisons. Data are presented as means ± SEM.
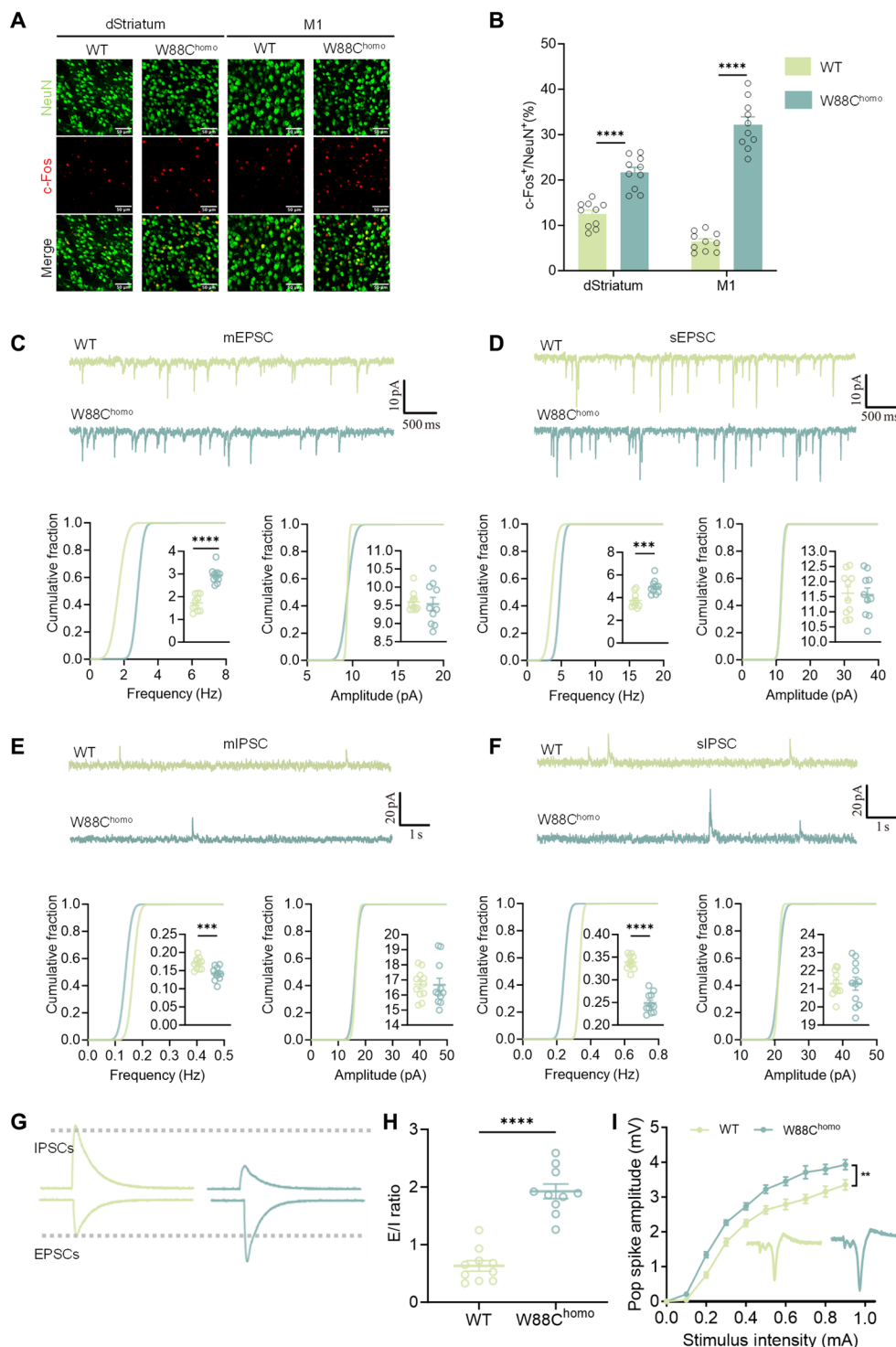
Fig. 5. Altered neuronal activation and synaptic dynamics in the striatal circuitry of W88C^homo male mice. (**A**) Confocal microscopy images reveal c-Fos (red) and NeuN (green) immunostaining in the dorsal striatum and M1 cortex. W88C^homo mice show increased c-Fos expression, indicating hyperactivity. (**B**) Quantitative analysis shows a significantly higher proportion of c-Fos–positive neurons in W88C^homo mice. (**C**) Traces of miniature excitatory postsynaptic currents (mEPSCs) from dorsal striatal spiny neurons demonstrate altered synaptic transmission in W88C^homo mice. (**D**) Spontaneous excitatory postsynaptic currents (sEPSCs) highlight differences in spontaneous excitatory activity between genotypes. (**E**) Miniature inhibitory postsynaptic currents (mIPSCs) indicate variations in inhibitory synaptic inputs. (**F**) Spontaneous inhibitory postsynaptic currents (sIPSCs) suggest modified inhibitory neurotransmission. (**G** and **H**) Comparison of traces and excitatory/inhibitory (E/I) ratios shows significant alterations. (**I**) Enhanced cortico-striatal pop spike amplitude in W88C^homo mice, as shown by extracellular field recordings. These results demonstrate significant changes and highlight the neural circuit alterations present in W88C^homo mice. Data are presented as means ± SEM. Sample sizes were $n = 10$ from three mice per group. Statistical analyses involved unpaired t-test and two-way ANOVA with Tukey's multiple comparisons test. Significance levels are indicated as n.s., $P > 0.05$; **$P < 0.01$; ***$P < 0.001$; ****$P < 0.0001$.

differences (fig. S13, E and F). We then performed whole-cell patch-clamp recordings on pyramidal neurons in the hippocampal regions of W88C[homo] and WT mice. The results showed no significant differences in the frequency and amplitude of mEPSCs/sEPSCs and mIPSCs/sIPSCs (fig. S14, A to D). This suggests that, although the W88C mutation affects binding with Dendrin in vitro, it does not have a notable effect in the mouse hippocampus, possibly due to in vivo compensatory mechanisms. This is consistent with the observation that W88C[homo] mice do not exhibit learning and memory impairments.

Neurodevelopmental disruptions in W88C[homo] mice linked to altered hippo pathway activity

Our investigation builds upon previous studies of the W88C mutation, exploring its potential effects on dopaminergic signaling and synaptic function. Our findings suggest that this mutation may have notable neurodevelopmental implications within the dorsal striatum, a region critically involved in TS pathology. Using Golgi staining, we assessed the neuronal architecture and observed marked morphological alterations in MSNs within the striatum. Sholl analysis revealed a significant increase in dendritic complexity in 1-month-old W88C[homo] mice (fig. S15, A and B), indicating disrupted synaptic connectivity essential for neural circuitry functionality. Furthermore, we observed similar findings in the MSNs of 3-month-old mice (fig. S16, A and B). Despite these complexities, spine density and PSD size appeared unaltered when compared with controls (fig. S15, C to G). To address whether W88C mutant mice exhibit the pathophysiological hallmarks of TS, we performed immunofluorescence staining to assess the abundance of specific striatal interneuron populations. We stained for NeuN (neuronal nuclei), PV (parvalbumin), and ChAT (choline acetyltransferase) in the striatum of both WT and W88C[homo] mice. Our analysis revealed no significant differences in the density of NeuN[+], PV[+], or ChAT^{+} cells between W88C[homo] mice and WT controls (fig. S17, A and B). This indicates that the W88C mutation does not lead to a reduction in these specific interneuron populations in the striatum.

Further, our study sheds light on the Hippo signaling pathway's involvement in these neurodevelopmental aberrations. The Hippo signaling pathway emerges as a pivotal role in orchestrating neuronal growth, morphogenesis, synaptic connectivity, functional maturity, and tissue homeostasis (41, 43–45). Kibra, a key modulator within this pathway, notably affects its regulatory functions (46). The influence of this pathway extends across multiple facets of neural development, encompassing neuronal proliferation and axonal and dendritic growth, predominantly through the modulation of its effector proteins, YAP (yes-associated protein) and TAZ (transcriptional coactivator with PDZ-binding motif) (47).

In W88C[homo] mice, we specifically assessed the impact of the mutation on the Hippo pathway. Western blot analysis of total tissue proteins from the striatal regions showed no significant differences in the levels of MST1 (mammalian STE20-like protein kinase 1), LATS1 (large tumor suppressor kinase 1), YAP1, and P-MST (phosphorylated MST) (Thr[183]) between W88C[homo] and WT mice (fig. S18, A and B). However, we observed elevated phosphorylation levels of LATS [P-LATS (Ser[909])] and YAP [P-YAP (Ser[127])] in W88C[homo] mice compared to those in WT (fig. S18, A and B). This finding indicates a heightened activation of the Hippo pathway in W88C[homo] mice, likely due to the effect of W88C mutation on Kibra, a known regulatory factor within this pathway (46). Kibra's interaction with LATS and its role in modulating LATS-mediated YAP phosphorylation (48) suggest that the W88C mutation enhances this interaction,

leading to increased phosphorylation and cytoplasmic accumulation of YAP, thus inhibiting its function as a transcriptional factor.

Given the early developmental period of mouse neurons and their cessation of development upon differentiation (49), as well as the involvement of multiple brain regions within the CSTC circuit in TS, we aimed to ensure the effectiveness of the rescue. Kibra is widely expressed throughout the CNS. On the basis of data from the Allen Mouse Brain Atlas (Allen Brain Atlas: Cell Types) and the Human Protein Atlas (single-cell type, WWC1), Kibra is predominantly expressed in various neuronal cells and astrocytes in both humans and mice. To further substantiate these findings, we extracted proteins from primary cultures of neurons, microglia, and astrocytes derived from mouse. Consistent with the database results, our data show that Kibra is highly expressed in neurons and astrocytes, while it is not expressed in microglia (fig. S19, A and B). Additionally, we confirmed this finding via in situ RNA hybridization in mouse brain tissue sections (fig. S19C). Given that our research focuses on alterations in neuronal dopamine signaling and morphology and that previous studies have implicated Kibra in synaptic plasticity, we chose to investigate the impact of WWC1 on the Hippo pathway specifically within neurons.

We investigated the effect of the Hippo pathway on the development of MSNs in W88C[homo] mice by performing lateral ventricular injections of adeno-associated virus (AAV) carrying neuron-specific promoters to overexpress WT WWC1 in postnatal day (P0) mice. Brain tissues were extracted at one month of age for analysis. Western blot analysis showed that overexpression of WT WWC1 in neurons rescued the alterations in Hippo pathway activity observed in W88C[homo] mice, as indicated by changes in phosphorylation levels of key pathway components (Fig. 6, A and B). Subsequently, we conducted Sholl analysis on MSNs in the dStriatum of mice using Golgi staining. We found that overexpression of WWC1 in W88C[homo] mouse neurons reduced the dendritic complexity of MSNs, but overexpression of WWC1 in WT mouse neurons did not affect the normal morphology of MSNs (Fig. 6, C and D). Meanwhile, we observed a decrease in the activation of neurons in the dStriatum and M1 after overexpression of WWC1 in W88C[homo] mice neurons, but not in WT mice (Fig. 6, E and F). DA2h dopamine fluorescent sensor recordings also showed that, after overexpressing WT-WWC1 in W88C[homo] mouse neurons, dopamine signals returned to normal levels, while WT mice remained unaffected (Fig. 6, G and H), with no changes in DA peak amplitude (Fig. 6, I and J).

Following the restoration of neuronal development and dopamine release in W88C[homo] mice, we investigated whether delivering WT-WWC1 to brain neurons would alter the behavioral phenotype. Overexpression of WT-WWC1 in W88C[homo] mouse neurons improved repetitive motor behaviors, increased movement distance in the open-field test, and reduced latency in the OF, EPM, YM, and pole climbing tests (Fig. 7, A to D). Next, we evaluated sensorimotor gating function in W88C[homo] mice. W88C[homo] mice with neuronal overexpression of WT-WWC1 showed significantly higher PPI compared to controls (Fig. 7E). Additionally, in social interaction tests, W88C[homo] mice with neuronal overexpression of WT-WWC1 exhibited significantly increased social interaction time (Fig. 7, F and G). However, overexpression of WT-WWC1 in WT mouse neurons did not affect the behavioral phenotype.

To verify the connection between Hippo pathway–related developmental disorders and TS-like behaviors, we injected a neuron-specific AAV virus overexpressing WT-WWC1 into the lateral ventricles of
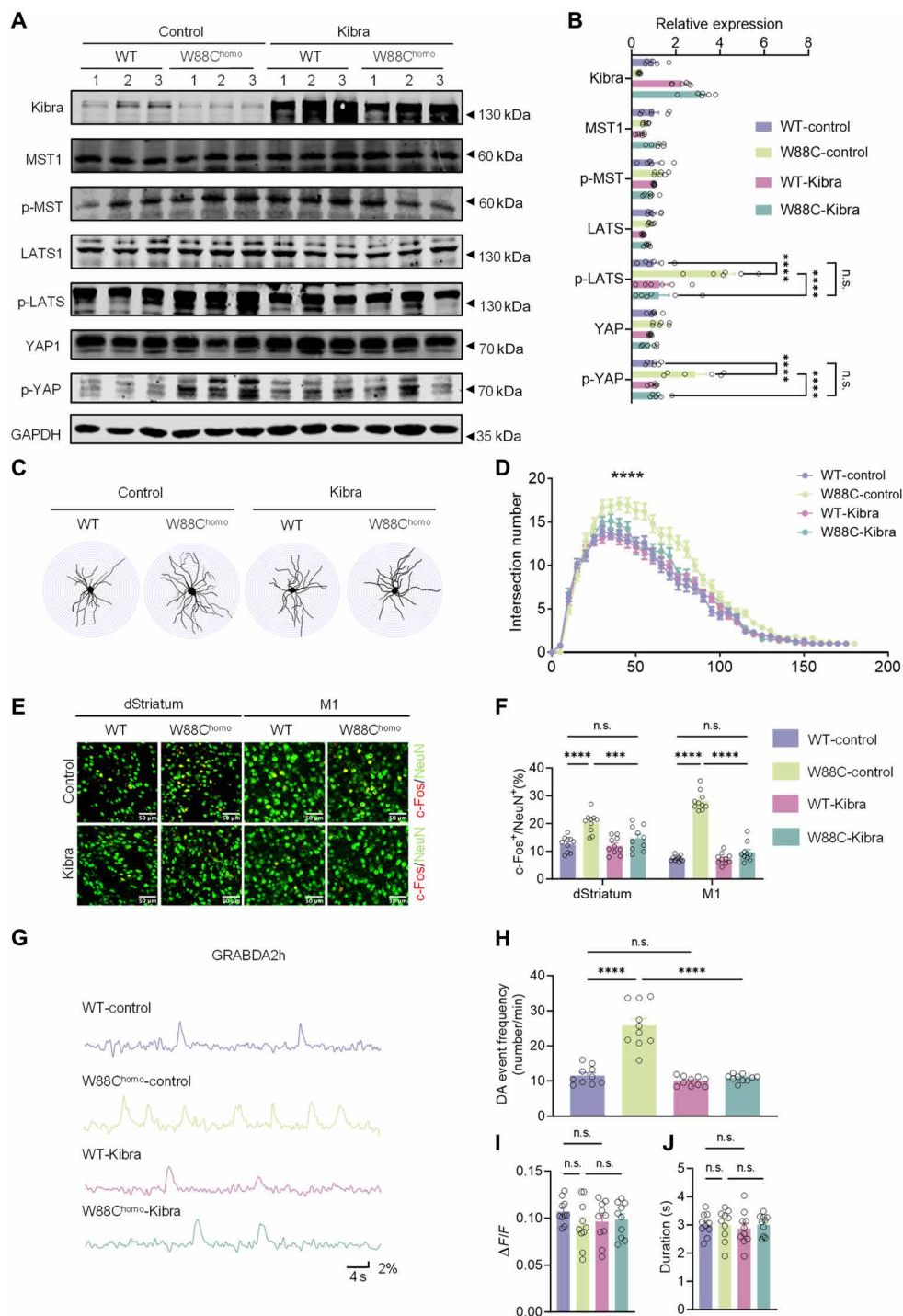
Fig. 6. Effects of brain-wide overexpression of Kibra on the Hippo pathway and the striatum in W88C^homo mice. (**A**) Western blots illustrating comparative levels of Kibra and other key hippo pathway proteins, namely, MST1, LATS1, YAP1, and their phosphorylated forms (p-MST, p-LATS, and p-YAP), in the brain tissue of WT and W88C^homo mice, with and without Kibra overexpression. (**B**) Quantification of protein expression changes. Data indicates significant overactivation of the hippo pathway in W88C^homo mice, which is mitigated by overexpression of Kibra. All protein expression levels are normalized to the values of the internal control protein. $n = 6$ mice per condition. (**C**) Illustrative dendritic complexity of MSNs via Golgi staining reconstructions in WT and W88C homozygous mice expressing Kibra. (**D**) Sholl analysis detailing dendritic branching intersections, indicating morphological changes in MSNs due to Kibra overexpression. $n = 50$ to 58 cells from six mice per condition. (**E**) Fluorescent imaging of c-Fos and NeuN immunostaining in dorsal striatum and M1 cortex, contrasting neuronal activation between WT and W88C homozygous mice. (**F**) Percentage of c-Fos positive neurons against NeuN, depicting changes in neuronal activity within key brain regions due to Kibra expression levels. $n = 10$ per group. (**G** and **H**) In vivo fiber photometry traces (G) and quantitative analysis (H) demonstrate elevated dopamine events in W88C^homo mice compared to those in controls, which are normalized by overexpression of Kibra. $n = 10$ per group. (**I** and **J**) Quantification of the peak $\Delta F/F$ (I) and the duration of dopamine events (J) indicates that there are no significant differences between any of the groups. $n = 10$ per group. n.s., $P > 0.05$; ***$P < 0.001$; ****$P < 0.0001$, two-way ANOVA with Tukey's multiple comparisons test. Data are all presented as means ± SEM.
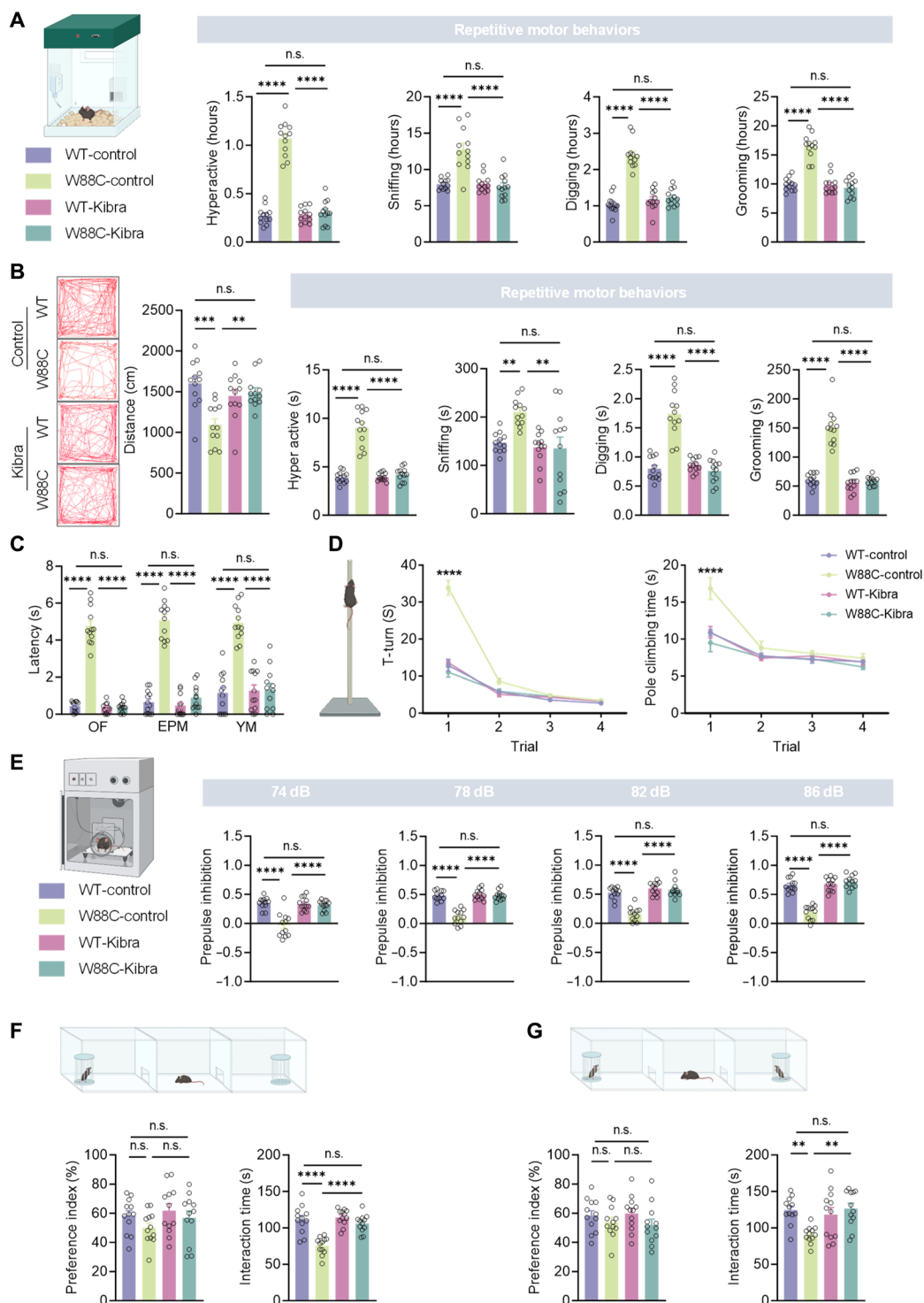
Fig. 7. Neuron-specific Kibra overexpression rescued TS-like behaviors in P0 W88C^homo male mice. (**A**) Spontaneous behavior analysis in the home cage reveals predominant repetitive behaviors such as hyperactivity, sniffing, digging, and grooming in W88C homozygotes. These behaviors are notably improved with Kibra overexpression. (**B**) Open-field trajectories and quantification of total distance show hypoactivity and increased repetitive motor activity during immobility in W88C^homo mice. Both measures are improved following Kibra intervention. (**C**) Behavioral assays demonstrate extended latency to action initiation, with delayed reactivity observed in the open field, elevated plus maze, and Y-maze tests, improved by Kibra overexpression. (**D**) Pole test results illustrate delayed responses in initial trials for W88C homozygotes, improved posttreatment. (**E**) PPI of the acoustic startle reflex indicates impairments in sensorimotor gating in W88C^homo mice that are ameliorated. PPI values are expressed as a proportion. (**F**) The three-chamber social test reveals a significant impairment in social ability in W88C^homo mice, with decreased interaction time, improved post-overexpression. (**G**) Social novelty assessments show no difference but decreased engagement time in W88C^homo mice, improved with Kibra intervention. Data are presented as means ± SEM. For all tests, $n = 12$ per genotype; statistical significance was determined using two-way ANOVA with Tukey's multiple comparisons test. Significance levels: n.s., $P > 0.05$; **$P < 0.01$; ***$P < 0.001$; ****$P < 0.0001$.

2-month-old mice and conducted assessments 3 weeks later. We analyzed the extent of viral infection in P0 and 2M (2 months) mice. Fluorescence imaging showed that the distribution of viral infection, as indicated by GFP expression, was similar in the cortex, striatum, hippocampus, and thalamus between P0 and 2M mice (fig. S20A). This suggests that the lateral ventricle injection led to effective and widespread infection in both age groups. Additionally, the colocalization with Neun confirmed the specificity of viral infection in neurons (fig. S20A). Quantitative analysis of Kibra RNA levels across different brain regions revealed no significant differences between the P0 and 2M groups (fig. S20B). Furthermore, the relative expression levels of overexpressed Kibra were comparable between P0 and 2M mice (Fig. 6, A and B, and fig. S21, A and B), demonstrating that the viral delivery method achieved consistent infection and expression levels across different developmental stages. Despite the reduced activation level of the Hippo pathway, reflected in the decreased phosphorylation levels of LATS and YAP (fig. S21, A and B), the TS-like behaviors in W88C[homo] mice did not improve (fig. S22, A to G).

These results indicate that overexpression of WT-*WWC1* in neurons during developmental stages can improve core TS-like behaviors in W88C[homo] mice, whereas overexpression in mature neurons has no effect. This finding suggests that the regulation of the developmental process by the Kibra-involved Hippo pathway is crucial for the manifestation of TS-like behaviors. The rescue effect observed during early development intervention highlights the specific contribution of the W88C mutation to the observed neurodevelopmental changes and offers a promising avenue for therapeutic intervention.

DISCUSSION

The exploration of TS poses notable challenges due to its complex etiology, involving intricate interactions among genetic, neurobiological, and environmental factors. Despite advancements in understanding TS, the integration of genetic risk factors with specific neurobiological pathways remains largely uncharted. Our study aimed to address this gap by investigating the W88C mutation in the *WWC1* gene, identified as a high-confidence risk gene for TS with a false discovery rate less than 0.1. The creation and analysis of the W88C[homo] mice have provided invaluable insights, linking this genetic alteration to specific neurodevelopmental and neurochemical changes (Fig. 8).

A critical aspect of our findings is the replication of core TS symptoms in W88C[homo] mice, particularly enhanced repetitive motor behaviors and sensorimotor gating deficits. Moreover, W88C[homo] mice exhibited a delayed response pattern before initiating actions. This hesitancy or prolonged processing time is analogous to the behavior observed in D1CT-7 model mice, which were engineered to simulate TS symptoms. These mice display a significant delay in initiating voluntary movements, which might involve multiple mechanisms including sensorimotor processing, motivational states, and anticipatory responses (*50*). W88C[homo] mice exhibited prolonged times in both the initiation and execution of the climbing task, which parallels the delayed reactivity and hesitancy observed in Slitrk1-mutant mice, a model with a gene associated with TS, when responding to appropriate behavior in new environments (*51*). In the social experiment, it was found that, while the W88C mutation did not affect the mice's social preferences, symptoms such as repetitive motor behaviors still interfered with their daily activities and social
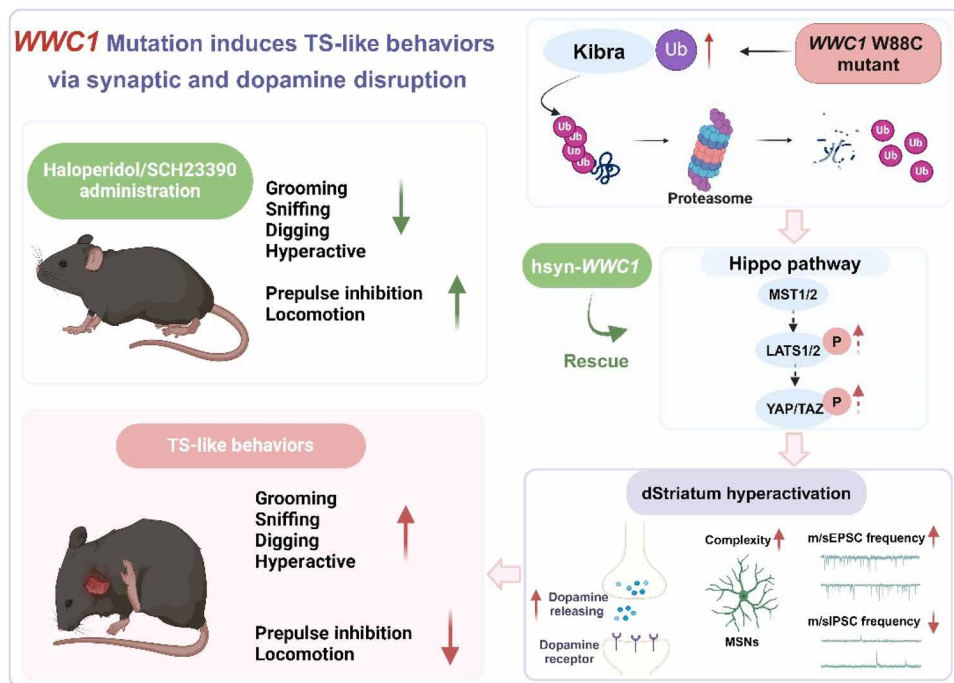

Fig. 8. Schematic illustration of synaptic and dopaminergic disruptions in *WWC1* mutation-induced TS-like behaviors. The W88C mutation in *WWC1* results in increased ubiquitination and degradation of the Kibra protein, leading to hyperactivation of the Hippo pathway, evidenced by elevated phosphorylation of Lats1/2 and YAP/TAZ. This overactivation causes developmental impairments, including increased dopamine release in the dorsal striatum, enhanced complexity of MSNs, and altered synaptic dynamics, which collectively contribute to hyperactivity in the dorsal striatum and the emergence of TS-like behaviors in mice. Treatment with the D2R antagonist haloperidol and D1R antagonist SCH23390 is shown to improve these behaviors.

interactions, consistent with the behavioral alterations observed in TS (6). This phenotypic manifestation is pivotal in validating the relevance of W88C mutation to TS. However, it is noteworthy that the model does not encompass all aspects of TS, particularly vocal tics, which presents an area for future refinement. W88C[homo] mice display a variety of behavioral characteristics that are associated with TS. These behaviors may reflect underlying mechanisms that are relevant to the complex pathophysiology of TS and its comorbidities. This makes it a valuable tool for studying the mechanisms of TS within a broader disease context and provides relevant insights that may also be applicable to OCD and ADHD.

The molecular underpinnings uncovered in our study, particularly the proteasome-mediated degradation of Kibra protein resulting from the W88C mutation, reveal a fresh pathophysiological mechanism in TS. This finding is notable as it connects a specific genetic mutation to a concrete molecular pathway, thereby providing a target for potential therapeutic intervention. The implication that altered protein degradation pathways may contribute to TS pathophysiology in the context of the W88C mutation opens fresh avenues in the quest for understanding specific molecular mechanisms in TS.

Furthermore, our study expands the discourse on the role of dopamine signaling in TS, unveiling a connection between *WWC1* mutations and dopamine signaling for the first time. Our findings demonstrate that D1R plays a notable role in the sensorimotor gating deficits observed in W88C[homo] mice, alongside the well-established role of D2R in TS pathophysiology. While D2R remains a primary target for TS treatment, our results suggest that the TS-like behaviors induced by abnormal dopamine release are not solely mediated by D2R.

Previous research highlighted the role of *WWC1* in synaptic plasticity regulation and postsynaptic component composition (13, 14), while Kibra was associated with controlling exosome secretion (52), suggesting the potential influence of W88C mutation on dopamine signaling intensity by affecting synaptic transmission. Our findings suggest that the W88C mutation may affect synaptic transmission in MSNs, which could potentially influence dopamine signaling. This observation may contribute to our understanding of neurotransmitter network regulation in TS.

The administration of haloperidol, a D2R antagonist, alleviated repetitive motor behaviors in W88C[homo] mice, mirroring its effects in patients with TS. However, it did not completely eliminate all TS-like symptoms. This observation helps explain why haloperidol can reduce repetitive motor behaviors in patients but cannot fully cure TS (53). Such neurochemical deviations, rectified by haloperidol and SCH23390, corroborate the dopaminergic dysregulation hypothesis, further validating our mouse model and highlighting the necessity of combination therapies for treating TS. While both sensors (dLight and GrabDA) are derived from D1R and D2R, respectively, and therefore could potentially be affected by their corresponding antagonist binding, our control experiments showed consistent results between behavioral and fluorescence measurements. Nevertheless, we acknowledge that future studies using alternative dopamine sensors could provide additional validation of these findings. This underscores the complex nature of TS pathophysiology and suggests that a multi-targeted approach, addressing both D1R and D2R systems, may be necessary for more comprehensive TS treatment strategies.

As the striatum plays a pivotal role in the CSTC circuitry associated with TS, the discovery of heightened dopamine signaling and altered synaptic transmission in the striatum led to the identification of morphological abnormalities in 90% of striatal neurons, known as MSNs (54). These morphological abnormalities, characterized by increased branching complexity, may alter the functional properties of MSNs. Such changes could potentially contribute to the altered striatal activity observed in TS (55), which might be associated with the manifestation of tics. The neurodevelopmental disruptions observed in W88C[homo] mice, underscore the importance of considering neurodevelopmental processes in TS pathology. The alterations in neuronal morphology and gene expression patterns linked to the Hippo signaling pathway provide insights into how genetic mutations might influence neurodevelopment, leading to TS symptoms. These findings prompt further exploration into the developmental trajectory of TS and how genetic factors might interact with neurodevelopmental processes.

Intriguingly, the W88C mutation leads to increased degradation of Kibra, and overexpression of WT Kibra in neuronal populations mitigated the hyperactivation of the Hippo signaling pathway engendered by the W88C mutation. This rescue effect contrasts with prior findings that posit Kibra as an activator of the Hippo pathway (43), proposing that Kibra may exert differential regulatory influences within neuronal contexts. This distinction underscores the potential for Kibra to interact with the Hippo pathway in a modulatory capacity that diverges from previously understood paradigms. Additionally, this indicates that the W88C mutation not only reduces Kibra expression level but also causes a gain of function in Kibra. However, it is important to note that Willsey *et al.* (10) also identified a stop-gain mutation in *WWC1* in TS (10), highlighting the complexity of *WWC1*'s role in TS and suggesting that both gain-of-function and loss-of-function mutations in this gene may contribute to TS pathophysiology, possibly through different mechanisms. This aligns with the observation that W88C[homo] mice do not exhibit significant learning and memory impairments, as previous studies have shown that knockdown of Kibra leads to deficits in these cognitive functions (14). Despite the association of Hippo pathway overactivation with neuronal apoptosis (56), our observations did not parallel an increase in apoptotic activity within the W88C[homo] mice. It leads us to infer that the primary repercussions of this dysregulated pathway extend to neurodevelopmental perturbations rather than cell survival, underscoring a fresh facet of Hippo pathway engagement in the neurodevelopmental trajectory of TS, a developmental neuropsychiatric disorder.

Our study, however, has certain limitations. While we have demonstrated the utility of the W88C[homo] mouse in replicating key aspects of TS, the absence of vocal tics highlights the challenge of fully recapitulating the human condition in a murine model. We have not examined the behavioral phenotype of aged W88C mutant mice, leaving it unclear whether the W88C mutation leads to notable learning and memory decline in old age due to increased degradation of Kibra. Additionally, it remains uncertain whether the Hippo pathway is the sole developmental regulatory pathway involving Kibra; the W88C mutation may affect other pathways, thereby amplifying its effects. Furthermore, the differences between various brain regions within the CSTC circuit involved in TS warrant further investigation. Moreover, focusing on a single genetic mutation, while valuable, does not encompass the polygenic and multifactorial nature of TS. Future studies should aim to incorporate these aspects to provide a more comprehensive understanding of the disorder.

Therefore, we compared our research with previously published studies on other TS mouse models (table S1). By comparing differences between various models, we provide a more comprehensive perspective on TS pathophysiology. Through this comparison, we identified several common features, enhancing the validity of our findings and their relevance to TS while also allowing us to assess each model's strengths and limitations in representing different aspects of TS. We have also observed that these studies reported motor and behavioral phenotypes in heterozygous mice, which aligns with the fact that most human patients with TS are heterozygous for the associated mutations. However, it is crucial to note that many of these models involve gene knockout operations or nonhuman mutation constructs designed to mimic symptoms, rather than directly simulating human disease mutations in mice. While these approaches may lead to more pronounced effects, they might also overlook some of the subtle impacts of human mutations. In contrast, our W88C homozygous mouse model directly incorporates a mutation found in human patients with TS. Although homozygous, this approach allows us to directly study the effects of a human TS-associated mutation in vivo. By comparing homozygous, heterozygous, and WT conditions, we can gain insights into gene dosage effects. We believe that studying both homozygous and heterozygous models is crucial for a comprehensive understanding of TS pathophysiology. Our homozygous model complements existing heterozygous models by potentially revealing effects that might be masked or subtle in heterozygous conditions. While we acknowledge the limitations of our homozygous model in directly representing the heterozygous state common in human TS, we believe that it offers valuable insights into the molecular mechanisms underlying the disorder, particularly in the context of the W88C mutation.

Notably, we observed that study by Nasello *et al.* (*57*) included the W88C mutation that we investigated in our current work. They detected some mild trends of TS-like behaviors in W88C mice but focused primarily on the Celsr gene without conducting an in-depth investigation of the W88C mutation. This may explain why they might have missed several potentially positive results. The study by Nasello *et al.* (*57*) indicated that male W88C^{hete} mice exhibited significantly increased activity levels in the open-field test, while female W88C^{hete} mice showed a trend toward decreased PPI. These findings appear to conflict with our results to some extent. However, in our investigation of W88C^{hete} mice, we observed that TS-like behaviors could be detected when recording after foot stimulation. This demonstrates that the phenotype of W88C^{hete} mice is unstable and not easily detectable. As we are different research teams using distinct experimental conditions, the level of stimulation applied to the mice and their sensitivity to the experimental environment may vary. This could potentially account for the differences in our results. Notably, while our W88C mouse model exhibits PPI deficits that are ameliorated by D1R antagonists, studies by Cadeddu *et al.* (*58*) and Nasello *et al.* (*57*) have shown that PPI deficits in other TS model mice, distinct from the W88C mutation, can be alleviated by haloperidol and aripiprazole (which act on D2R and 5-HT receptors). This distinction underscores the complexity and potential heterogeneity of dopaminergic signaling dysregulation in TS. Although our findings suggest a notable role for D1R signaling in PPI deficits within the W88C model, they should not be interpreted as implying that all PPI deficits in TS are uniquely linked to D1R signaling. Rather, the differences between these models and the divergent mechanisms of drug action highlight the likelihood of multiple

pathways of dopaminergic dysregulation in TS. However, our W88C^{homo} mouse model successfully integrates PPI deficits with D1R receptors, auditory startle response, and dopaminergic signaling, providing an effective approach for future detailed investigations into the molecular mechanisms underlying PPI abnormalities.

Our research not only performed a comprehensive behavioral screening of W88C mice but also revealed the mutation's impact on Kibra expression levels and explored the underlying molecular mechanisms. These findings align with our previous research showing that the W88C mutation leads to protein instability. This suggests that, while the W88C point mutation mice generated by Nasello *et al.* (*57*) and our group were created using the CRISPR method, subtle differences in housing conditions, handling practices, or experimental protocols between laboratories may have contributed to the variations in outcomes. This emphasizes not only the potential impact of differences in genetic construction strategies but also the critical role of environmental and experimental factors in determining experimental results.

Understanding model-specific effects can inform more personalized treatment approaches based on patients' genetic profiles. We believe that this comparative approach notably enhances the scientific value and clinical relevance of our study. By integrating data from multiple models, we can construct a more comprehensive and robust framework for understanding TS pathophysiology.

In conclusion, the W88C^{homo} mouse represents a notable advancement in TS research, offering a unique perspective on the disorder's genetic, neurobiological, and neurodevelopmental dimensions. Our findings not only enhance the understanding of TS but also pave the way for the development of targeted therapeutic strategies. This study contributes to the broader scientific effort in deciphering the complexities of neurodevelopmental disorders, emphasizing the need for integrated approaches that combine genetic, neurobiological, and developmental perspectives.

Our study provides important insights into the effects of the *WWC1* mutation on dopaminergic signaling and neuronal morphology in W88C^{homo} mice. However, further research is needed to fully elucidate the specific mechanisms underlying these alterations. A particularly promising direction for future studies would be to investigate the differential effects of the *WWC1* mutation on D1R- and D2R-expressing MSNs. Additionally, it would be valuable to explore whether the dysregulation of dopamine dynamics seen in W88C^{homo} mice can be reversed by upregulating Kibra in adulthood. Addressing these questions could provide further insight into the cell-type–specific mechanisms of the *WWC1* mutation and offer potential therapeutic strategies for disorders like TS. These future studies will help clarify the role of dopamine signaling in the structural and functional changes observed in W88C^{homo} mice and advance our understanding of the broader implications of *WWC1* dysfunction in neuropsychiatric conditions.

MATERIALS AND METHODS
Experimental design
Animals
Mice were bred and reared under the same conditions in accordance with institutional guidelines and the Animal Care and Use Committee of the Animal Core Facility at Huazhong University of Science and Technology (Wuhan, China). All experiments were conducted in strict accordance with the guidelines of animal research ethics

and were approved by the National Natural Science Foundation of China, with the approval number 32200795. All animals were housed in groups of three to five mice per cage under a 12-hour light-dark cycle (8:00 a.m. to 8:00 p.m.) at a consistent ambient temperature (21° ± 1°C) and humidity (50 ± 5%) with food and water ad libitum. All behavior experiments were conducted during the light phase of the cycle. W88C^homo mice were generated on the C57BL/6J background by CRISPR-Cas9 CRISPR-Cas9–mediated Extreme Genome Editing system (Beijing Biocytogen). Cas9–guide RNA (gRNA) target sequences were meticulously designed to precisely target regions spanning exon 2-3 or 3-4, strategically inducing DNA breaks to facilitate homologous recombination. In a meticulously orchestrated procedure, in vitro–transcribed Cas9 mRNA, gRNA, and oligo donors carrying the intended mutations (p.W88C, c.G264T) were co-injected into fertilized mouse eggs. For genotyping purposes, a set of primers was used, exemplifying the precision of the experimental design as follows: forward: TGGTTGTGTGACA-AATCCTGGTGGA and reverse: ACTCAGTGTGGATAGTCCCT-GCTGT. All mice were genotyped and assigned a number 3 weeks after birth.

All experiments were conducted by researchers who were systematically blinded to the genotypes and treatment groups of the mice. This blinding procedure was maintained throughout data collection, processing, and manual verification to ensure unbiased assessment and interpretation of the results.

Behavior
Age-matched cohorts of mice were used for all experiments. Each cohort began testing at ~1 to 2 months of age and completed the full behavioral testing battery by 3 to 4 months of age. For any given test, all mice within and across cohorts were of the same age. Before the initiation of the experiment, the mice underwent daily handling for a minimum of 3 days to acclimate to the experimenter. Subsequently, they were transferred to the testing room and allowed a minimum of 1 hour for acclimation before the commencement of the tests.

Home-cage behavior
To assess the natural exploratory motivation and repetitive behaviors of mice, individual testing was conducted with video recording in the PhenoTyper home cages (40 cm by 40 cm by 40 cm, Noldus, Holland), which provided a home-like environment for mice, complete with ample food and water supply. Mice were introduced into the PhenoTyper home cages at 10:00 a.m. in a room maintained under a 12-hour light/12-hour dark cycle, with controlled air conditions. Following a 24-hour habituation period, locomotion and spontaneous behaviors were monitored by detecting infrared beam interruptions caused by the animals' movements over a 48-hour period. Automated video analysis using EthoVisionXT software (Noldus, Holland) was used to quantify individual behaviors.

Prepulse inhibition
Mice were subjected to the PPI paradigm using the SR-LAB system (San Diego Instruments, San Diego, CA, USA) to assess their sensorimotor gating capabilities. The experimental setup comprised individual startle chambers, each consisting of a nonrestrictive Plexiglas cylinder placed on an illuminated, ventilated sound-attenuating chamber. Acoustic stimuli, generated by a high-frequency speaker positioned 33 cm above the cylinder, induced movements in the mice, which were monitored and transduced via a piezoelectric accelerometer beneath the cylinder. The resultant data underwent digitization and storage facilitated by a computer and interface assembly.

Mouse movements, particularly vertical displacements induced by startle responses, were transformed into a voltage trace using a piezoelectric transducer beneath the platform. Startle amplitude, representing the peak-to-peak maximum startle magnitude within a 1-s window post–acoustic stimulation, served as the quantitative measure. The experiment incorporated five trial types, characterized by distinct configurations of broadband auditory stimuli presented against a 65-dB background. "Pulse-alone" trials, featuring a 40-ms broadband 120-dB noise burst, established a baseline for startle responses. "Prepulse" trials, categorized into four types, entailed an identical 120-dB startle pulse preceded by a 20-ms broadband prepulse occurring 100 ms before the startle pulse, with intensities 9, 13, 17, or 21 dB above background. "No-stimulus" trials solely comprised the background noise, providing insight into spontaneous mouse movement. The experimental session commenced with a 5-min acclimation period, during which only the background noise was presented. Subsequent trials were organized into four continuous blocks, with an average separation of 15 s (range, 7 to 23 s) between consecutive trials. Blocks 1 and 4 exclusively featured six consecutive pulse-alone trials, while blocks 2 and 3 comprised six pulse-alone trials, five of each prepulse trial type, and five no-stimulus trials, arranged in a pseudorandom sequence. The entire 23-min session encompassed 74 test trials. Criteria for data exclusion involved trials with excessive spontaneous movement, a noisy baseline, or an inadequate response to the startle stimulus. The PPI was computed for each prepulse intensity using the formula: [(Startle on pulse-alone trials) − (Startle on prepulse trials)]/(Startle on pulse-alone trials) × 100%.

Open-field test
An open-field arena measuring 50 cm by 50 cm by 38 cm was used with a digital camera on the top to monitoring the activities of the mice. The open-field test was conducted for a total duration of 10 min. At the beginning of the test, each mouse was gently placed in a corner of the open-field arena and allowed to freely explore the entire area for the full 10-min period. The TopScan tracking software EthoVision XT (Noldus, Holland) was used to analyze the number of entries and the time spent in the center, defined as a 20 cm–by–20 cm square region.

Elevated plus maze test
The apparatus comprises two open arms (6-cm width by 63-cm full length) positioned opposite each other, with 0.5-cm-tall ledges and two closed arms of the same size featuring 15-cm-high walls. The junction area of the four arms measures 6 cm in width and 6 cm in length. At the commencement of each test, mice were centrally placed in the apparatus, facing one of the open arms. Subsequently, their behaviors were recorded for 5 min using a camera. The TopScan tracking software EthoVision XT (Noldus, Holland) was used for the automatic analysis of behavioral parameters, including the number of entrances and time spent in both open and closed arms.

Rotarod tests
Mice underwent training for three consecutive days and were subsequently subjected to accelerating rotarod tests. During the training trail, the rotarod experiment was conducted with mice undergoing a protocol that involved a gradual acceleration from 4 to 30 rpm within the initial 2 min, followed by a consistent speed of 30 rpm maintained for the subsequent 3 min. This cycle was repeated four times, with each trial lasting 5 min. Each animal underwent testing sessions with an 8-min interval between each trial for recovery. During the test trial, a timer was positioned beside the experimenter.

During each run, the experimenter recorded the time at which each mouse fell off the rotarod. Task failure was defined as the inability of mice to remain on the rotating bar for more than 10 s on three consecutive attempts.

Sucrose preference test

Two water bottles labeled A and B filled with a 1% (w/v) fresh sucrose solution were prepared before the experiment. The animals were housed in their respective home cages and initially trained to consume from both bottles for 24 hours. After the training phase, bottle A was replaced with tap water, while bottle B with a 1% (w/v) fresh sucrose solution remained. The test spanned 2 days, and, to eliminate any position bias, the positions of bottles A and B were switched on the second day.

The weight of each bottle was measured both before and after the sucrose preference test. The sucrose preference was calculated using the formula: Sucrose preference (%) = Sucrose intake/(Sucrose intake + Water intake) × 100%.

Tail suspension test

The mice were individually suspended by the tails in a tail suspension test apparatus made of white plastic, measuring 50 cm in height, 30 cm in width, and 25 cm in depth. A suspension bar with a diameter of 1 cm was securely fixed at the top of the apparatus. A digital camera was used to capture the behaviors of the mice during a 6-min duration. Subsequently, the immobility time during the last 4 min was analyzed using the EthoVision XT software (Noldus, Holland), which uses TopScan technology to track movements.

Data from the test were excluded from analysis if a mouse caught its tail with its paws. Immobility was defined as the period during which the mouse hung passively or remained motionless.

Morris water maze

We used a swimming pool with a diameter of 1.5 m for mice, filled with white, nontoxic ink water, and maintained the temperature at 25°C. Before the training session, mice were placed in the behavior room where they were housed for 1 to 2 days. The training session spanned 6 days, with specific instructions for each day. On the first day, mice were allowed to rest on the platform for 30 s and had 90 s to locate the hidden platform. If they failed to find the platform within 90 s, then they would be guided to the platform and required to stay for an additional 30 s. Throughout the training session, each animal performed a total of four trials, with the mouse released from four different randomized points in the pool. Following the 6-day training session, the mouse underwent a one-probe trial the hidden platform was removed, and the time spent in each quadrant and the number of crossings over the original platform area were recorded and analyzed.

Y-maze

The Y-maze, with a Y-shaped configuration comprising three arms and a central zone, was used in the experiment. Each arm was randomly assigned as the start for individual mice. The start and novel arms were randomized for each mouse. Mice were then placed at the end of any one arm of the Y-maze and allowed to explore for 8 min freely.

The TopScan tracking software EthoVision XT (Noldus, Holland) was used to record and analyze the behavior of the animals throughout the entire 8-min duration. The recorded parameters included the total number of entries into the maze arms (total number of entries) and the occurrence of sequential and consecutive entries into all three arms of the Y-maze in a single round (alternation). The spontaneous alternation behavior score was calculated as follows: (Alternations/Total number of entries) × 100%.

Novel object recognition

To assess performance in the object recognition task, mice underwent two sessions, each consisting of one trial: the acquisition and retrieval trials. During the acquisition trial, mice were placed in an arena containing two identical objects for 10 min. Mice that did not explore the objects for at least 20 s within these 10 min were excluded from further experiments. Exploration was defined as a mouse approaching its nose within 1 cm of the object, involving looking, sniffing, or touching. The retrieval session occurred 2 hours after the acquisition trial. In this trial, one of the objects presented in the first trial was replaced with a novel object (differed in shape and color but were made of the same materials and had similar general dimensions). Mice were then placed back in the arena for 10 min, and the total time spent exploring each object was recorded. Objects and arenas were thoroughly cleaned with 70% ethanol between trials, and the introduction of new objects and their placement were counterbalanced across all experiments to avoid bias. Motor activity and the time spent in active exploration of familiar or novel objects during the retrieval trial were calculated. The recognition index was defined as follow: (Time spent exploring the novel object)/(Total time exploring both objects) × 100%.

Three-chamber social test

In the three-chamber social test system, the evaluation of sociability (measured as spending more time in the chamber with a stranger mouse compared to that in the empty chamber) and social novelty (indicated by more time spent in the chamber with a novel mouse than with a familiar mouse) is conducted. The rectangular apparatus measures 102 cm in length, 47 cm in width, and 45 cm in height. This design features two side cross walls, each with a width of 10 cm, facilitating unrestricted movement for mice between chambers. Initially, a 10-min random exploration phase is initiated, where mice freely navigate the central chamber. After a 1-hour interval, the sociability test is executed: A stranger mouse (stranger I) is introduced into a wire cage placed in either the left or right chamber, while an identical empty wire cage is placed in the opposite chamber. Mice are again placed in the central chamber for a 10-min exploration period. Following another 1-hour interval, the social novelty test is conducted: a novel mouse (stranger II) is introduced into the previously empty wire cage, while the initially encountered mouse (stranger I, familiar mouse) remains in its cage. The subject mouse explores the entire social test arena for a 10-min session. Notably, the criteria for defining exploration involve mice approaching their nose within 2.5 cm of the object.

To quantify the results, two indices are used. The recognition index is calculated as follows: Recognition index = [Time_stranger/(Time_stranger + Time_empty)] × 100%. Additionally, the recognition discrimination index is determined using the following formula: Recognition discrimination index = [Time_novel − Time_familiar/(Time_novel + Time_familiar)] × 100%.

Contextual discrimination tests

In FC, two distinct contexts, referred to as context A and context B, are used. On the initial day of the experiment, subjects are initially situated in context A. Following a 3-min acclimatization period, they undergo a sequence of five tone-shock pairings. The aversive stimulus, delivered as a shock at 0.5 mA for 2 s, occurs 18 s after the cessation of the tone, which is characterized by parameters of 75 dB,

2-kHz frequency, and a duration of 20 s. Notably, each conditioned stimulus (CS)–unconditioned stimulus (US) pairing includes an empty trace interval positioned between the termination of the tone and the initiation of the shock.

On the second day, mice are placed in context B, distinguished by novel olfactory cues, floor texture, and visual cues for 5 min, no CS or US is presented. Following this exposure to context B, on the third day of the experiment, mice are returned to the original context A for 5 min without the presentation of any CS or US. On the last day of the experiment, mice are reintroduced to context A for a 3-min duration. During this phase, three-tone presentations are administered, each devoid of any accompanying shocks. Freezing behavior is operationally defined as the complete absence of motion sustained for a minimum duration of 0.75 s. The recorded time spent in a frozen state during each designated period is subsequently reported as a measure of conditioned fear response.

Pole test
Mice are placed on a rough ball, the lower end of which is connected to a wooden rod with a rough surface and a circular cross section. The lower end of the rod is positioned inside the mouse cage, and their descent is observed to determine whether they descend facing upward or with their backs facing up. By recording the time taken for the mouse to slide from the top to the bottom, along with their posture and subsequent movements, the experiment aims to assess the mouse's motor coordination. Each mouse undergoes four trials, and there was a 10-min interval between each experimental trial, allowing for sufficient recovery time for the mice between runs. The time taken for the climbing sessions is measured.

Quantitative real-time PCR
RNA was extracted from brain tissue using TRIzol (Invitrogen, catalog no. 15596026) and subsequently reverse transcribed according to the manufacturer's protocol with the QuantiTect Reverse Transcription kit (QIAGEN, catalog no. 205311). Quantitative reverse transcription–PCR was conducted on an ABI PRISM 7000 Sequence Detection System using the SYBR Premix Ex Taq II Kit (TAKARA, catalog no. RR820A). The primer sequences used were as follows: forward: 5′-CACCACCAGCTGGATCGAC-3′ and reverse: 5′- CGAGGATC-CAGAGACCAAGC-3′.

Nissl staining
After fixation and dehydration, brain tissue was sectioned into 30-µm-thick slices. The slices were washed with distilled water for 2 min twice. Staining was performed at 37°C for 15 min, followed by dehydration in 95% ethanol for two cycles of 2 min each. The sections were then immersed in xylene for 5 min for clearing. Last, the neutral resin was used for mounting, covered with a coverslip, and, once the resin cured, imaging was conducted using an Olympus VS120 to visualize neuronal cell bodies.

H&E staining
Skin tissue samples were embedded in paraffin and sectioned into 5- to 10-µm slices, which were placed on microscope slides and dried. The slides were then immersed in xylene for 5 to 10 min to remove the paraffin, followed by rehydration through a graded series of ethanol (100, 95, 80, and 70%) for 2 to 3 min each, and rinsed with distilled water. The sections were stained with hematoxylin for 5 to 10 min and washed in running water for 5 to 10 min. Subsequently, the slides were stained with eosin for 30 s to 2 min and then rinsed with distilled water. The sections were then dehydrated through a graded series of ethanol (70, 80, 95, and 100%) for 2 to 3 min each and cleared in xylene for 5 to 10 min. Last, the sections were mounted with neutral resin, and, once the resin cured,

imaging was performed using an Olympus VS120 to achieve clear visualization of tissue morphology and cellular details.

Toluidine blue staining
Skin tissue samples were embedded in paraffin and sectioned into 5- to 10-µm slices, which were placed on microscope slides and dried. The slides were immersed in xylene for 5 to 10 min to remove the paraffin, followed by rehydration through a graded ethanol series (100 and 70%) for 2 to 3 min each, and rinsed with distilled water. The sections were stained in 0.1% toluidine blue O solution for 5 to 10 min and then gently rinsed with distilled water to remove excess dye. Dehydration was performed using a gradient of ethanol (70 and 100%) for 2 to 3 min each, and, if necessary, the sections were cleared in xylene for 5 to 10 min. Last, the neutral resin was used for mounting, and, after curing, imaging was conducted with an Olympus VS120.

Immunohistochemistry
Mice were deeply anesthetized with an overdose of isoflurane and were transcardially perfused with 100 ml of phosphate-buffered saline (PBS; pH 7.4), followed by 4% paraformaldehyde (PFA). Brains were then extracted and postfixed in 4% PFA for 24 hours. Coronal sections (30 µm) were prepared using a cryostat microtome (Leica) at −20° (Wetzlar, Germany). Immunohistochemistry was conducted on free-floating brain sections according to previously established methods. In brief, brain sections were first blocked with blocking solution containing 3% normal goat serum in 0.1 M PBS with 0.3% Triton X-100 at room temperature for 1 hour with agitation and then incubated in primary antibodies diluted in blocking solution overnight at 4°C with agitation. The following primary antibodies were used: mouse anti-NeuN (1:300; Millipore, MAB377), rabbit anti–c-Fos (1:200; Synaptic Systems, 226008), goat anti-ChAT (1:100; Millipore, AB144P), mouse anti-PV (1:500; Swant, PV235), mouse anti-glial fibrillary acidic protein (GFAP; 1:1000; Cell Signaling Technology, 3670), and rabbit anti-Iba1(ionized calcium-binding adapter molecule 1) (1:1000; Wako, 019-19741). The second day, sections were subsequently rinsed and incubated with conjugate-adsorbed Alexa Fluor 488 donkey anti-mouse (Invitrogen, A-32766), Alexa Fluor 555 donkey anti-mouse (Invitrogen, A-31570), Alexa Fluor 488 donkey anti-rabbit (Invitrogen, A-21206), Alexa Fluor 555 donkey anti-rabbit (Invitrogen, A-32794), and Alexa Fluor 647 donkey anti-goat (Invitrogen, A-21447) at room temperature for 1 hour. Following the labeling procedure, sections were rinsed, air-dried, and cover slipped. Double labeling was observed and imaged using a confocal laser-scanning microscope (Fluoview FV3000, Olympus). Images were processed with ImageJ. Cell counting was done on maximum intensity projection.

Sequentially immerse the sections in xylene I for 15 min, xylene II for 15 min, absolute ethanol I for 5 min, absolute ethanol II for 5 min, 85% ethanol for 5 min, and 75% ethanol for 5 min and, lastly, wash with distilled water. Place citrate buffer solution (pH 6.0) in a pressure cooker and heat until boiling. Insert the slides on a heat-resistant plastic rack into the pressure cooker, heat for 3 min, and then open the pressure relief valve and lid. During this process, prevent excessive evaporation of the buffer; avoid drying the slides. After natural cooling, place the slides in PBS (pH 7.4) and wash on a decolorizing shaker three times, each for 5 min. Use a microwave retrieval box with citrate buffer solution (pH 6.0) at medium heat for 5 min. Allow to cool naturally afterward. Prepare a 3% H_2O_2 solution with water, immerse the sections in it, and incubate at room temperature for 20 min. If the tissue tends to detach from the slide, consider reducing the concentration of H_2O_2 and the incubation time. Wash with PBS three times, each for 5 min. Use a histochemical

pen to draw a circle around the tissue and then apply serum onto the tissue, and incubate at 37°C for 30 min. Use serum from the same source as the secondary antibody (usually 10% goat serum) for blocking. Dilute the primary antibody with antibody dilution buffer, remove excess serum from the slide, apply the antibody working solution to the tissue, and incubate overnight at 4°C or for 2 hours at 37°C. The following primary antibodies were used: rabbit anti-CD45 (1:200; Abcam, ab40763). Prepare the secondary antibody (biotinylated anti-rabbit secondary antibody; 1:200; VectorLabs, BA-1100) with PBST (PBS with Tween 20), apply an appropriate amount to the tissue, and incubate at 37°C for 1 hour. Wash the slides with PBST three times, each for 5 min. Apply DAB (3,3′-diaminobenzidine) working solution to the tissue; observe under a microscope and, when specific brown expression appears, rinse off the DAB staining solution from the tissue with water; and then immerse the slides in water. The expression is typically brown, with a lighter or even colorless background. Immerse the slides in hematoxylin staining solution for 3 to 5 min, rinse off excess hematoxylin with water, and, once the nucleus turns blue, place the slides in 0.5% hydrochloric acid alcohol differentiation solution for 1 to 2 s, and immediately rinse with water. Then, place the slides in bluing solution for 3 to 5 s and rinse with water. At this point, the cell nuclei should be blue, with no apparent blue in other areas. Sequentially immerse the slides in tanks containing absolute ethanol I, absolute ethanol II, absolute ethanol III, butanol I, butanol II, xylene I, and xylene II, each for 5 min. Remove the slides, air-dry, and apply an appropriate amount of neutral resin over the tissue. Cover with a coverslip and allow to dry.

For immunofluorescence quantification, six coronal sections per mouse were collected at 250-μm intervals from bregma +1.10 mm to −0.15 mm. Images were acquired under identical parameters. Cell counting was performed using a semiautomated approach in ImageJ software by experimenters blinding to experimental conditions. After background subtraction and threshold adjustment, the "Analyze Particles" function was applied with unified parameters: cell size (100 to 5000 pixel^2) and circularity (0.3 to 1.0). For identification of ChAT$^+$, NeuN$^+$, and PV$^+$ neurons, colocalization with 4′,6-diamidino-2-phenylindole (DAPI) signal was analyzed using ImageJ colocalization plugin to ensure counted positive cells contained intact nuclei. The automated counts were visually verified and manually corrected if necessary to ensure accuracy. For whole striatal analysis, ChAT$^+$, NeuN$^+$, and PV$^+$ neurons colocalized with DAPI were quantified within anatomically defined striatal boundaries. For colocalization analysis of c-Fos/NeuN in the dorsal striatum and M1 cortex, the dorsal striatum was delineated using the anterior commissure as the ventral boundary, and M1 cortex was identified on the basis of standard anatomical coordinates. Both total cell numbers and the percentage of marker-positive cells were calculated. The reliability of the semiautomated analysis was verified by manual recounts of 25% of samples by a second observer (interobserver agreement > 90%).

RNAscope in situ hybridization combined with immunohistochemistry

Mice were anesthetized and perfused with PBS followed by 4% PFA. Brain tissues were carefully extracted and fixed in 4% PFA for 24 hours. Subsequently, the tissues were embedded in optimal cutting temperature compound and sectioned into 15- to 20-μm thick slices using a cryostat. The sections were adhered to SuperFrost slides and allowed to dry at room temperature and stored at −80°C until further use. Before experimentation, slides were washed twice with distilled water for 2 min

each and then dried at 60°C for 30 min. The RNAscope multichannel second-generation fluorescence combined with immunofluorescence detection was performed following the manufacturer's instructions [Advanced Cell Diagnostics (ACD), Hayward, CA, USA]. Briefly, dried tissue sections were fixed in 4% PFA at 4°C for 15 min, followed by dehydration in a series of ethanol solutions (50, 70, 95, 100, and 100%) for 5 min each, with brief rinses using ultrapure water between each pretreatment step. Following a 10-min treatment with hydrogen peroxide at room temperature, the sections were incubated in a target retrieval reagent for 5 min. After retrieval, the sections were washed three to five times with PBST. A hydrophobic barrier was drawn around each section, and 150 to 200 μl of diluted primary antibodies (NeuN, GFAP, and Iba1) were applied. The slides were placed in a humidified chamber at 4°C overnight. The following day, the sections underwent hybridization using the HybEz hybridization system (ACD). Sections were washed twice with PBST for 2 min each and fixed again with 4% PFA for 30 min, followed by two additional washes with PBST. The sections were treated with RNAscope Protease Plus at 40°C for 30 min. Mouse Wwc1 RNAscope probe (ACD, catalog no. 439391) was applied, alongside negative (ACD, catalog no. 320871) and positive (ACD, catalog no. 320881) control probes, and hybridized at 40°C for 2 hours. Amplification steps were carried out as per the manufacturer's guidelines, with washing steps using 1× wash buffer between each amplification stage. Detection was performed using TSA Vivid Fluorophore 570 (ACD, catalog no. PG-323272). After the final in situ hybridization horseradish peroxidase blocking step, a secondary antibody conjugated to DAM488/DAR488 was applied and incubated at room temperature for 30 min. Slides were then washed twice with PBST for 2 min each, followed by a 30-s incubation with DAPI for nuclear staining. After drying, the slides were observed using an FV3000 confocal microscope.

Plasmid construction, cell culture, and transfections

The expression constructs for *Homo sapiens WWC1*^{WT}-GFP and *WWC1*^{W88C}-GFP were provided by M. Zhang (Southern University of Science and Technology, Shenzhen, China). The expression constructs for murine *WWC1*^{WT}-GFP and *WWC1*^{W88C}-GFP were amplified and cloned into the pTGFP vector plasmids. HEK293T cells were cultured in Dulbecco's modified Eagle's medium (DMEM) supplemented with 10% FBS and 1% penicillin/streptomycin at 37°C with 5% CO$_2$. Cell transfections were conducted post-plating using Neofect DNA transfection reagent, following the manufacturer's instructions [Neofect (Beijing) Biotech].

Primary neuronal culture

Embryos were harvested at embryonic day (E15) to E16 for primary neuronal culture as previously described (*59*). Cerebral cortices were dissected in pre-cold Hanks' balanced salt solution (HBSS) and then dispersed in 0.025% trypsin (diluted with HBSS) at 37°C for 20 min with gentle shaking every 5 min. At the last 5 min, deoxyribonuclease (DNase) I was added. After digestion, the supernatant was removed and replaced with HBSS to halt the enzymatic activity. Neurons were dissociated by gentle pipetting 10 times and then plated onto poly-D-lysine (PDL)–coated coverslips in a neurobasal medium supplemented with 10% FBS, 2% B27, and 1% GlutaMAX. The cells were allowed to settle for 3 hours at 37°C in 5% CO$_2$. Subsequently, the neurons were incubated in a neurobasal medium supplemented with 2% B27, 1% GlutaMAX, and 1% penicillin/streptomycin at 37°C and 5% CO$_2$. Half of the medium was replaced every 4 to 5 days to maintain cell viability and functionality.

Cultured primary microglia and astrocyte

Mixed glial was from P1 to P3 mouse pups. Cortical regions were dissected and isolated, and the meninges were removed in pre-cold HBSS. The tissue was then trypsinized with 0.05% trypsin-EDTA (diluted with HBSS) for 20 min at 37°C with gentle shaking every 5 min. At the last 5 min, DNase I was added. Cells were neutralized with two volumes of complete media (DMEM and 10% FBS) and centrifuged for 5 min. After discarding the supernatant, cells were resuspended with full volumes of complete media and plated on PDL-coated T75 flasks with complete medium. Medium was granulocyte-macrophage colony-stimulating factor (5 ng/ml) 2 days later and kept for 10 days. Half of the medium was replaced every 4 to 5 days. Floating microglia were collected from the mixed glia by shaking the flask at 225 rpm for 2 hours. Astrocyte was collected after the mixed glia by shaking the flask at 225 rpm for 18 hours and trypsinized with 0.05% trypsin-EDTA.

Western blot and IP

For brain tissues, they were swiftly dissected and homogenized in a prechilled lysis buffer [10 mM tris-Cl (pH 7.6), 50 mM NaF, 1 mM Na3VO4, and 1 mM EDTA] after decapitations, supplemented with a protease inhibitor cocktail (BIMAKE). The homogenates underwent rapid homogenization using a cryogenic grinder for 60 s at 55 Hz, repeated twice. Subsequently, 4× sample buffer [200 mM tris-Cl (pH 7.6), 8% SDS, and 40% glycerol] was added to the lysates. The supernatant was collected through centrifugation and determined protein concentration using a BCA kit (Pierce, Rockford, IL). The samples were mixed with a final concentration of 10% β-mercaptoethanol and 0.05% bromophenol blue, followed by boiling for 5 min. For cells, after washing twice with 1× PBS, proteins were extracted using radioimmunoprecipitation assay (RIPA) buffer (Beyotime) supplemented with protease inhibitor Cocktail (BIMAKE). The cell extracts underwent sonication on ice for three cycles of 5 s each. Subsequently, cell lysates were combined with one-third volume of 4× sample buffer for cells [composed of 0.2 M tris-HCl at pH 6.8, 10% SDS, 40% glycerol, 0.03% bromophenol blue, and 5% β-mercaptoethanol) and then subjected to boiling for 5 min. Protein separation was accomplished through SDS–polyacrylamide gel electrophoresis (PAGE) using a 10% gel, followed by transfer onto nitrocellulose membranes (GE Healthcare Bio-Sciences). Membranes were then blocked with 5% skim milk or BSA (for phosphorylated proteins) for 1 hour at room temperature and subsequently incubated with primary antibodies overnight at 4°C. After three thorough washes, membranes were exposed to IRDye 800CW secondary antibodies (LI-COR Biosciences) for 1 hour at room temperature and scanned using the Odyssey CLX Infrared Imaging System. Protein bands were analyzed using ImageJ software.

For IP experiments, cells were lysed with pre-cold mild RIPA buffer (P0013D, Beyotime Biotechnology) supplemented with a protease inhibitor cocktail (BIMAKE) on ice for 30 min. The lysates were then centrifuged at 12,000g for 15 min at 4°C. The supernatants were mixed with 10 μl of protein A+G Beads [MCE (MedChemExpress)] and rotated for 10 min at 4°C to remove nonspecific bindings. For Kibra IP, the supernatants were incubated with anti-GFP at 4°C for 8 to 12 hours, followed by the addition of 50 μl of protein A+G Beads (MCE) and rotation at 4°C for 4 hours. The immunoprecipitate was eluted from the magnetic beads by boiling in 4× sample buffer for 5 min and subjected to SDS-PAGE and immunoblotting.

The following primary antibodies were used: rabbit polyclonal anti-KIBRA (1:1000; ABclonal, A17110); mouse monoclonal anti-ubiquitin (1:1000; Cell Signaling Technology, 3936); rabbit polyclonal anti-MST1 (1:750; ABclonal, A18100); rabbit monoclonal anti–p-MST1 (Thr[183])/MST2 (Thr[180]) (1:1000; Cell Signaling Technology, 49332); rabbit polyclonal anti-LATS1 (1:750; ABclonal, A17992); rabbit polyclonal anti–p-LATS1 (Ser[909]) (1:1000; Cell Signaling Technology, 9157); rabbit monoclonal anti-YAP1 (1:2000; ABclonal, A21216); rabbit monoclonal anti–p-YAP (Ser[127]) (1:1000; Cell Signaling Technology, 13008S); rabbit monoclonal anti-PSD95 (1:1000; Cell Signaling Technology, 3450S); rabbit polyclonal anti-NR2A (1:1000; Cell Signaling Technology, 4205); rabbit monoclonal anti-PKM1 (1:750; ABclonal, A21052); rabbit polyclonal anti-NR2B (1:1000; Cell Signaling Technology, 4207); rabbit polyclonal anti-GLUR1 (1:750; ABclonal, A1826); rabbit monoclonal anti-GLUR2 (1:750; ABclonal, A11316); rabbit monoclonal anti-PKCα (1:750; ABclonal, A11107); rabbit monoclonal anti-NeuN (1:1000; Cell Signaling Technology, 24307); rabbit polyclonal anti-Iba1 (1:1000; Wako, 019-19741); mouse monoclonal anti-GFAP (1:1000; Cell Signaling Technology, 3670); mouse monoclonal anti–glyceraldehyde-3-phosphate dehydrogenase (1:200,000; Proteintech, 60004-1-Ig); mouse monoclonal anti–β-actin (1:60,000; Proteintech, 66009-1-Ig); IRDye 800CW donkey anti-mouse immunoglobulin G (IgG) secondary antibody (1:15,000; LI-COR, 926-32212); and IRDye 800CW donkey anti-rabbit IgG secondary antibody (1:15,000; LI-COR, 926-32213).

Electron microscopy

Mice were anesthetized with an overdose of isoflurane and perfused with PBS followed by 4% PFA. Following postfixation, the samples were immersed in a 4% glutaraldehyde solution at 4°C for 3 days. The samples underwent sequential washes in 7.5% sucrose and 0.1 M sodium cacodylate buffer and were then postfixed in 1% osmium tetroxide for 2 hours with initial microwave treatment for 6 min. After two 20-min washes in 0.11 M veronal acetate buffer, the samples were en bloc stained in 1% uranyl acetate in distilled water for 1 hour, followed by two 20-min washes in 0.11 M veronal acetate buffer. Dehydration of the samples was carried out using serial dilutions of ethanol [70, 95, and 100% (2×)] for 20 min each, with an initial microwave treatment of 2 min. The samples were then treated twice for 20 min with propylene oxide and impregnated with a 50:50 mixture of propylene oxide and Epon resin overnight at 4°C, with initial microwave treatment for 3 min. Next, the samples were impregnated with 100% Epon resin and subjected to three changes, each lasting 2 hours, with initial microwave treatment for 3 min each. The tissue samples were embedded in molds and incubated for 48 hours at 60°C. Afterward, semi-thin sections (0.5 μm) were cut and stained with 0.8% toluidine. Thin striatal sections (70 nm) were then cut, mounted on grids, and post-stained with uranyl acetate and Sato's lead citrate. Grids were examined using a Philips CM 12 transmission electron microscope at ×40,000 magnification. Images were acquired and PSD measurements were performed using ImageJ by an observer blinded to the sample genotypes.

Whole-cell patch clamp

Male mice aged 30 ± 2 days were anesthetized with isoflurane and decapitated. The brains were placed and sliced in ice-cold modified artificial cerebrospinal fluid (ACSF; 124 mM NaCl, 3.0 mM KCl, 2.0 mM CaCl2, 1.2 mM MgCl2·6H2O, 1.25 mM Na2HPO4, 26 mM NaHCO3, and 10 mM glucose) and saturated with 95% O2 and 5% CO2. A vibratome (DSK Microslicer; Leica) was used to cut 300-μm brain sections. The slices underwent a 15-min incubation at 32°C in oxygenated saturated ACSF, followed by a 1-hour incubation at room temperature before recordings, and then transferred to a

recording chamber and constantly perfused with oxygenated ACSF at 22°C (1.5 to 2.0 ml/min).

The striatum and individual MSNs were visualized and identified with a fluorescent infrared differential interference contrast Axioskop 2FS upright microscope equipped with a Hamamatsu C2400-07E infrared camera by location, shape, and size.

sEPSCs and mEPSCs were recorded using an internal solution containing 140 mM potassium gluconate, 10 mM Hepes, 2 mM NaCl, 0.2 mM EGTA, 2 mM Mg^{2+} adenosine 5′-triphosphate (ATP), and 0.3 mM Na guanosine 5′-triphosphate, along with an external solution containing 10 μM bicuculline. An additional presence of 1 μM tetrodotoxin (TTX) was added for mEPSCs. Similarly, sIPSCs and mIPSCs were recorded using an internal solution containing 153.3 mM CsCl, 10 mM Hepes, 1 mM $MgCl_2$, 5 mM EGTA, 4 mM Mg^{2+} ATP, and an external solution containing 20 μM 6-cyano-7-nitroquinoxaline-2,3-dione, and 50 μM APV. An additional presence of 1 μM TTX was added for mIPSCs. A gap-free model with a detection threshold set at 6 pA (2.5 times the SD of the noise) and analyzed with Clampfit 10.2 software (Axon Instruments, Union City, CA, USA).

Evoked E/I ratio: IPSCs were recorded at 0 mV, and EPSCs were recorded at −60 mV. Stimulating electrode filled with regular ACSF was placed at the inner border of the corpus callosum between the cortex and dstriatum, while the recording electrode was positioned in the dstriatum, ~400 to 450 μm away from the stimulating electrode. A range of stimulus intensities was applied to generate input-output (I-O) curves for both EPSCs and IPSCs. Only the responses within the linear range of the I-O curves (i.e., where the E/I ratio was stable) were used to calculate the evoked E/I ratio. On average, recordings were obtained from two cells per slice, with two to three slices collected from each mouse.

Extracellular field recording

A platinum-iridium concentric bipolar stimulating electrode was placed at the inner border of the corpus callosum between the cortex and dstriatum to predominantly activate cortical axons. Borosilicate glass recording electrodes filled with 2 M NaCl were positioned in the dstriatum ~400 to 450 μm from the stimulating electrode. Corticostriatal field population spikes were evoked with 0.15-ms step depolarizations at 0.5 mA intensity at a frequency of 0.05 to 0.1 Hz. Baseline responses were monitored to ensure stable population spike amplitude for a minimum of 5 min. I-O functions were then determined for the population spike amplitude through three consecutive rounds of stimulation from 0 to 1.0 mA in 0.1-mA increments. Population spike amplitude was measured as the average of early peak positivity to peak negativity and from peak negativity to late peak positivity.

Cell filling

Mice were deeply anesthetized with an overdose of isoflurane and subsequently perfused with PBS followed by 4% PFA. The brains were then postfixed overnight in 4% PFA. Coronal sections of 200 μm were obtained using a vibratome and stored in PBS at 4°C. Selected brain slices were mounted on a tissue stage for further processing. MSNs in the dorsal striatum were targeted and confirmed based on their morphology and spine density. Micropipettes loaded with Lucifer Yellow dye (Sigma-Aldrich, L-0259) were used to impale the cell bodies, and dye delivery was facilitated by applying a continuous 10-nA current for 5 min using a micropipette containing 0.1 M LiCl solution. Following cell filling, sections were incubated in blocking solution containing rabbit anti–Lucifer Yellow antibody (1:500; Invitrogen, A5750) for 3 days at 4°C, followed by incubation with

biotinylated goat anti-rabbit antibody (1:500; Vector Laboratories, BA-1000) at room temperature for 2 hours. After washing twice, sections underwent a tertiary incubation with streptavidin-conjugated Alexa Fluor 488 (1:1000; Invitrogen, S11223). Last, sections were mounted on slides and imaged using confocal microscopy. Spine density was quantified by manually counting and classifying dendritic protrusions from secondary dendrites.

Fiber-optic recording in freely moving mice

One-month-old WT and W88C[homo] mice underwent intracranial injections with a 1-μl volume of AAV2/9-hSyn-DA2h [1×10^{12} vg (viral genomes)/ml], precisely targeted at the dorsal striatum with coordinates of 0.44 mm from bregma, 2 mm from the midline, and 3.2 mm vertical from the cortical surface. Subsequently, the optical fiber probes (inner core diameter of 200 mm and fiber numerical aperture of 0.37; Inper, Shanghai) with an outer diameter of 1.25 mm and an optical fiber length of 3.5 mm were surgically implanted 0.20 mm above the injection site and sealed with dental cement. Three weeks post-surgery (to allow the mice to recover and to allow for virus expression), fiber-optic recordings were conducted in an open-field apparatus, using the 470-nm lasers (DPSS laser, Inper Co. Ltd.). Mice were connected to the recording equipment through Fiber Photometry (410/470) (Inper). Signals were acquired at a frame rate of 50 Hz, with an exposure time of 9 ms, with gain 0, using 470-nm light at 30 to 40% power. The analog voltage signals were digitalized and collected using the FiberPhotometry software (Inper Plot) and further analyzed in MATLAB. The fluorescence responses were calculated as ($F_{raw} − F_{baseline}$)/$F_{baseline}$. Peaks of fluorescence response more than a threshold (3.5 baseline SD) was defined as DA signal events (DA events).

Real-time dopamine monitoring during PPI testing

One-month-old WT and W88C[homo] mice received intracranial injections of 1 μl of AAV2/9-hSyn-dLight1.1 (1×10^{12} vg/ml), precisely targeted at the dorsal striatum (coordinates: 0.44 mm from bregma, 2 mm from midline, and 3.2 mm vertical from the cortical surface). Optical fiber probes (inner core diameter of 200 mm and fiber numerical aperture of 0.37) were implanted 0.20 mm above the injection site. PPI testing was conducted using a modified SR-LAB system (San Diego Instruments, San Diego, CA, USA). A small hole was made in the top of the standard PPI test chamber to allow for fiber-optic connection. Mice were gently restrained in a modified Plexiglas cylinder with a small opening at the top, allowing the optical fiber to pass through and connect with the mouse. Dopamine signal recording was performed using a fiber photometer (410/470) (Inper). Signals were acquired at a frame rate of 50 Hz, with an exposure time of 9 ms, gain set to 0, using 470-nm light at 30 to 40% power. Dopamine signal data were collected using FiberPhotometry software (Inper Plot) and analyzed in MATLAB. Simultaneously, PPI responses were recorded using the SR-LAB system. The PPI protocol, calculation formula, and the formula for fluorescence response calculation were the same as described in the Fiber-optic recording in freely moving mice and Prepulse inhibition sections. Dopamine signal events were aligned with PPI event times for analysis.

Golgi staining

Golgi staining was conducted on dissected brains using the FD Rapid GolgiStain Kit (PK401) following the manufacturer's instructions (FD NeuroTechnologies, Columbia, MD, USA). The procedure involved immersing brain tissues in a mixture of solution A and solution B for 2 weeks at room temperature, shielded from light, with a solution

change after the initial 24 hours. Subsequently, the tissues were transferred to solution C and kept in darkness for 3 to 7 days, with another solution change after the first 24 hours.

Following the staining process, the brains were serially sectioned at 150 μm using a vibrating microtome from Leica, Germany. The resulting slices underwent a 10-min wash in a solution composed of solution D and solution E. Afterward, the slices were rinsed with double-distilled water, followed by dehydration using graded alcohols (50, 75, and 95% ethanol). Last, the slices were subjected to three rounds of clearing in xylene and mounted using a resinous medium, completing the Golgi staining procedure. This method allows for the visualization and analysis of neuronal morphology and architecture in stained brain tissues.

Intracerebroventricular injections

Bilateral intracerebroventricular injections were conducted on P0 mouse pups. Neonatal P0 mice were positioned on an ice-cold plate subjected to cryoanesthetized, then using a 10-μl Hamilton syringes to penetrate the skull just posterior to bregma and 2 mm lateral to the midline. AAV2/9 virus (2 μl) containing 10^{12} viral genomes/ml was injected into the ventricle. The addition of Fast Green dye (1 mg/ml; Sigma-Aldrich) to the virus solution facilitated the visualization of successful injections. Following injection, the needle was slowly retracted, and the P0 pups were allowed to recover fully on a warming blanket before being returned to their cages and were kept with their parent until they were weaned.

Stereotaxic AAV injection

For stereotaxic injection, mice were subjected to anesthesia through intraperitoneal administration of a ketamine and xylazine mixture. Subsequently, they were secured in a mouse head holder. Following this, openings were surgically created above the striatum field to facilitate the bilateral injection of AAVs (AAV2/9) at a concentration of 10^{12} viral genomes per milliliter (vg/ml), precisely targeted at the lateral ventricle (coordinates: −0.22 mm from bregma, ±1.0 mm from midline, and 2.2 mm vertical from the cortical surface). The AAV2/9 encoding hSyn-*WWC1* used were intended for *WWC1* overexpression, while relative control viruses encoding GFP were concurrently administered.

Statistical analysis

To ensure unbiased data processing, all statistical analyses were performed by researchers who were blind to group allocation until analyses were completed. Statistical analyses were performed using GraphPad Prism 9 (GraphPad software). Two-sample comparisons were assessed through unpaired *t* tests, and the data are reported as means ± SD or SEM. For multiple group comparisons, one-way analysis of variance (ANOVA) followed by Tukey's test was used to ascertain statistical significance. In the context of comparing each group to a control group, one-way ANOVA with Dunnett's multiple comparison tests was used. Bonferroni's post hoc test was applied following two-way ANOVAs, contingent upon meeting assumptions of normality and equal variance (*F* test). All data were presented as means ± SEM. Statistical significance was denoted as *$P < 0.05$, **$P < 0.01$, ***$P < 0.001$, and ****$P < 0.0001$.

Supplementary Materials

The PDF file includes:
Figs. S1 to S22
Table S1
Legends for movies S1 and S2

Other Supplementary Material for this manuscript includes the following:
Movies S1 and S2

REFERENCES AND NOTES

1. M. E. Hirschtritt, P. C. Lee, D. L. Pauls, Y. Dion, M. A. Grados, C. Illmann, R. A. King, P. Sandor, W. M. McMahon, G. J. Lyon, D. C. Cath, R. Kurlan, M. M. Robertson, L. Osiecki, J. M. Scharf, C. A. Mathews, Tourette Syndrome Association International Consortium for Genetics, Lifetime prevalence, age of risk, and genetic relationships of comorbid psychiatric disorders in tourette syndrome. *JAMA Psychiatry* **72**, 325–333 (2015).

2. J. Bliss, D. J. Cohen, D. X. Freedman, Sensory experiences of Gilles de la Tourette syndrome. *Arch. Gen. Psychiatry* **37**, 1343–1347 (1980).

3. T. Knight, T. Steeves, L. Day, M. Lowerison, N. Jette, T. Pringsheim, Prevalence of tic disorders: A systematic review and meta-analysis. *Pediatr. Neurol.* **47**, 77–90 (2012).

4. J. M. Scharf, L. L. Miller, C. A. Gauvin, J. Alabiso, C. A. Mathews, Y. Ben-Shlomo, Population prevalence of Tourette syndrome: A systematic review and meta-analysis. *Mov. Disord.* **30**, 221–228 (2015).

5. J. Joseph, Tourette's syndrome. *N. Engl. J. Med.* **345**, 1184–1192 (2001).

6. K. K. Set, J. N. Warner, Tourette syndrome in children: An update. *Curr. Probl. Pediatr. Adolesc. Health Care* **51**, 101032 (2021).

7. T. Pringsheim, C. Ganos, J. F. McGuire, D. Hedderly, D. Woods, D. L. Gilbert, J. Piacentini, R. C. Dale, D. Martino, Rapid onset functional tic-like behaviors in young females during the COVID-19 pandemic. *Mov. Disord.* **36**, 2707–2713 (2021).

8. T. Paulus, T. Bäumer, A. Verrel, A. Weissbach, V. Roessner, C. Beste, A. Münchau, Pandemic tic-like behaviors following social media consumption. *Mov. Disord.* **36**, 2932–2935 (2021).

9. D. Mataix-Cols, K. Isomura, A. Pérez-Vigil, Z. Chang, C. Rück, K. J. Larsson, J. F. Leckman, E. Serlachius, H. Larsson, P. Lichtenstein, Familial risks of tourette syndrome and chronic tic disorders: A population-based cohort study. *JAMA Psychiatry* **72**, 787–793 (2015).

10. A. J. Willsey, T. V. Fernandez, D. Yu, R. A. King, A. Dietrich, J. Xing, S. J. Sanders, J. D. Mandell, A. Y. Huang, P. Richer, L. Smith, S. Dong, K. E. Samocha, B. M. Neale, G. Coppola, C. A. Mathews, J. A. Tischfield, J. M. Scharf, M. W. State, G. A. Heiman, De novo coding variants are strongly associated with tourette disorder. *Neuron* **94**, 486–499.e9 (2017).

11. Z. Lin, Z. Yang, R. Xie, Z. Ji, K. Guan, M. Zhang, Decoding WW domain tandem-mediated target recognitions in tissue growth and cell polarity. *eLife* **8**, e49439 (2019).

12. L. K. Jacobsen, M. R. Picciotto, C. J. Heath, W. E. Mencl, J. Gelernter, Allelic variation of calsyntenin 2 (CLSTN2) modulates the impact of developmental tobacco smoke exposure on mnemonic processing in adolescents. *Biol. Psychiatry* **65**, 671–679 (2009).

13. T. E. Tracy, P. D. Sohn, S. S. Minami, C. Wang, S.-W. Min, Y. Li, Y. Zhou, D. Le, I. Lo, R. Ponnusamy, X. Cong, B. Schilling, L. M. Ellerby, R. L. Huganir, L. Gan, Acetylated tau obstructs KIBRA-mediated signaling in synaptic plasticity and promotes tauopathy-related memory loss. *Neuron* **90**, 245–260 (2016).

14. L. Makuch, L. Volk, V. Anggono, R. C. Johnson, Y. Yu, K. Duning, J. Kremerskothen, J. Xia, K. Takamiya, R. L. Huganir, Regulation of AMPA receptor function by the human memory-associated gene KIBRA. *Neuron* **71**, 1022–1029 (2011).

15. L. Anuj, R. P. Arivazhagan, A. Surabhi, A. Kanakarajan, S. Sundaram, R. S. Pitani, L. Mudduwa, J. Kremerskothen, G. Venkatraman, S. K. Rayala, KIBRA attains oncogenic activity by repressing RASSF1A. *Br. J. Cancer* **117**, 553–562 (2017).

16. Z. Ji, H. Li, Z. Yang, X. Huang, X. Ke, S. Ma, Z. Lin, Y. Lu, M. Zhang, Kibra modulates learning and memory via binding to Dendrin. *Cell Rep.* **26**, 2064–2077.e7 (2019).

17. T. Deckersbach, T. Chou, J. C. Britton, L. E. Carlson, H. E. Reese, J. Siev, L. Scahill, J. C. Piacentini, D. W. Woods, J. T. Walkup, A. L. Peterson, D. D. Dougherty, S. Wilhelm, Neural correlates of behavior therapy for Tourette's disorder. *Psychiatry Res.* **224**, 269–274 (2014).

18. L. C. Baldan, K. A. Williams, J.-D. Gallezot, V. Pogorelov, M. Rapanelli, M. Crowley, G. M. Anderson, E. Loring, R. Gorczyca, E. Billingslea, S. Wasylink, K. E. Panza, A. G. Ercan-Sencicek, K. Krusong, B. L. Leventhal, H. Ohtsu, M. H. Bloch, Z. A. Hughes, J. H. Krystal, L. Mayes, I. de Araujo, Y.-S. Ding, M. W. State, C. Pittenger, Histidine decarboxylase deficiency causes tourette syndrome: Parallel findings in humans and mice. *Neuron* **81**, 77–90 (2014).

19. R. L. Albin, J. W. Mink, Recent advances in tourette syndrome research. *Trends Neurosci.* **29**, 175–182 (2006).

20. M. R. DeLong, Putamen: Activity of single units during slow and rapid arm movements. *Science* **179**, 1240–1242 (1973).

21. J. W. Mink, The basal ganglia: Focused selection and inhibition of competing motor programs. *Prog. Neurobiol.* **50**, 381–425 (1996).

22. J. P. Bolam, J. J. Hanley, P. A. C. Booth, M. D. Bevan, Synaptic organisation of the basal ganglia. *J. Anat.* **196**, 527–542 (2000).

23. T. V. Maia, V. A. Conceição, Dopaminergic disturbances in tourette syndrome: An integrative account. *Biol. Psychiatry* **84**, 332–344 (2018).

24. A. E. Rusheen, J. Rojas-Cabrera, A. Goyal, H. Shin, J. Yuen, D.-P. Jang, K. E. Bennet, C. D. Blaha, K. H. Lee, Y. Oh, Deep brain stimulation alleviates tics in tourette syndrome via striatal dopamine transmission. *Brain* **146**, 4174–4190 (2023).

25. M. Salery, P. Trifilieff, J. Caboche, P. Vanhoutte, From signaling molecules to circuits and behaviors: Cell-type–specific adaptations to psychostimulant exposure in the striatum. *Biol. Psychiatry* **87**, 944–953 (2020).

26. M. M. Robertson, Tourette syndrome, associated conditions and the complexities of treatment. *Brain* **123**, 425–462 (2000).

27. S. Liu, M. Tian, F. He, J. Li, H. Xie, W. Liu, Y. Zhang, R. Zhang, M. Yi, F. Che, X. Ma, Y. Zheng, H. Deng, G. Wang, L. Chen, X. Sun, Y. Xu, J. Wang, Y. Zang, M. Han, X. Wang, H. Guan, Y. Ge, C. Wu, H. Wang, H. Liang, H. Li, N. Ran, Z. Yang, H. Huang, Y. Wei, X. Zheng, X. Sun, X. Feng, L. Zheng, T. Zhu, W. Luo, Q. Chen, Y. Yan, Z. Huang, Z. Jing, Y. Guo, X. Zhang, C. P. Schaaf, J. Xing, C. Wang, F. Yu, J.-S. Guan, Mutations in ASH1L confer susceptibility to tourette syndrome. *Mol. Psychiatry* **25**, 476–490 (2020).

28. M. Engeln, Y. Song, R. Chandra, A. La, A. M. E. Fox, B. Evans, M. D. Turner, S. Thomas, T. C. Francis, R. Hertzano, M. K. Lobo, Individual differences in stereotypy and neuron subtype translatome with TrkB deletion. *Mol. Psychiatry* **26**, 1846–1859 (2021).

29. K. D. Gadow, J. Roohi, C. J. DeVincent, E. Hatchwell, Association of ADHD, tics, and anxiety with dopamine transporter (DAT1) genotype in autism spectrum disorder. *J. Child Psychol. Psychiatry* **49**, 1331–1338 (2008).

30. E. F. Halff, G. Rutigliano, A. Garcia-Hidalgo, O. D. Howes, Trace amine-associated receptor 1 (TAAR1) agonism as a new treatment strategy for schizophrenia and related disorders. *Trends Neurosci.* **46**, 60–74 (2023).

31. L. J. Mosher, R. Frau, A. Pardu, R. Pes, P. Devoto, M. Bortolato, Selective activation of D 1 dopamine receptors impairs sensorimotor gating in long–evans rats. *Br. J. Pharmacol.* **173**, 2122–2134 (2016).

32. M. A. Geyer, Are cross-species measures of sensorimotor gating useful for the discovery of procognitive cotreatments for schizophrenia? *Dialogues Clin. Neurosci.* **8**, 9–16 (2006).

33. S. Khoja, L. Asatryan, M. W. Jakowec, D. L. Davies, Dopamine receptor blockade attenuates purinergic P2X4 receptor-mediated prepulse inhibition deficits and underlying molecular mechanisms. *Front. Cell. Neurosci.* **13**, 331 (2019).

34. A. P. F. Chen, L. Chen, K. W. Shi, E. Cheng, S. Ge, Q. Xiong, Nigrostriatal dopamine modulates the striatal-amygdala pathway in auditory fear conditioning. *Nat. Commun.* **14**, 7231 (2023).

35. G. Horga, A. Abi-Dargham, An integrative framework for perceptual disturbances in psychosis. *Nat. Rev. Neurosci.* **20**, 763–778 (2019).

36. M. G. Kutlu, J. E. Zachry, P. R. Melugin, J. Tat, S. Cajigas, A. U. Isiktas, D. D. Patel, C. A. Siciliano, G. Schoenbaum, M. J. Sharpe, E. S. Calipari, Dopamine signaling in the nucleus accumbens core mediates latent inhibition. *Nat. Neurosci.* **25**, 1071–1081 (2022).

37. A. P. F. Chen, J. M. Malgady, L. Chen, K. W. Shi, E. Cheng, J. L. Plotkin, S. Ge, Q. Xiong, Nigrostriatal dopamine pathway regulates auditory discrimination behavior. *Nat. Commun.* **13**, 5942 (2022).

38. N. R. Swerdlow, D. L. Braff, V. L. Masten, M. A. Geyer, Schizophrenic-like sensorimotor gating abnormalities in rats following dopamine infusion into the nucleus accumbens. *Psychopharmacology* **101**, 414–420 (1990).

39. L. C. Baldan Ramsey, M. Xu, N. Wood, C. Pittenger, Lesions of the dorsomedial striatum disrupt prepulse inhibition. *Neuroscience* **180**, 222–228 (2011).

40. V. S. Sohal, J. L. R. Rubenstein, Excitation-inhibition balance as a framework for investigating mechanisms in neuropsychiatric disorders. *Mol. Psychiatry* **24**, 1248–1257 (2019).

41. J. Stepan, D. E. Heinz, F. Dethloff, T. Bajaj, A. Zellner, K. Hafner, S. Wiechmann, S. Mackert, Y. Mecdad, M. Rabenstein, T. Ebert, S. Martinelli, A. S. Häusl, M. L. Pöhlmann, A. Hermann, X. Ma, H. Pavenstädt, M. V. Schmidt, A. Philipsen, C. W. Turck, J. M. Deussing, B. Kuster, M. C. Wehr, V. Stein, J. Kremerskothen, C. T. Wotjak, N. C. Gassen, Hippo-released WWC1 facilitates AMPA receptor regulatory complexes for hippocampal learning. *Cell Rep.* **41**, 111766 (2022).

42. K. Kauppi, L.-G. Nilsson, R. Adolfsson, E. Eriksson, L. Nyberg, KIBRA polymorphism is related to enhanced memory and elevated hippocampal processing. *J. Neurosci.* **31**, 14218–14222 (2011).

43. D. Kandilya, S. Shyamasundar, D. K. Singh, A. Banik, M. P. Hande, W. Stünkel, Y. S. Chong, S. T. Dheen, High glucose alters the DNA methylation pattern of neurodevelopment associated genes in human neural progenitor cells in vitro. *Sci. Rep.* **10**, 15676 (2020).

44. K. O. Rojek, J. Krzemień, H. Doleżyczek, P. M. Boguszewski, L. Kaczmarek, W. Konopka, M. Rylski, J. Jaworski, L. Holmgren, T. J. Prószyński, Amot and Yap1 regulate neuronal dendritic tree complexity and locomotor coordination in mice. *PLOS Biol.* **17**, e3000253 (2019).

45. S. Schoch, A. Quatraccioni, B. K. Robens, R. Maresch, K. M. J. van Loo, S. Cases-Cunillera, T. Kelly, T. Opitz, V. Borger, D. Dietrich, J. Pitsch, H. Beck, A. J. Becker, Ste20-like kinase is critical for inhibitory synapse maintenance and its deficiency confers a developmental dendritopathy. *J. Neurosci. Off. J. Soc. Neurosci.* **41**, 8111–8125 (2021).

46. L. Wang, K. Choi, T. Su, B. Li, X. Wu, R. Zhang, J. H. Driskill, H. Li, H. Lei, P. Guo, E. H. Chen, Y. Zheng, D. Pan, Multiphase coalescence mediates hippo pathway activation. *Cell* **185**, 4376–4393.e18 (2022).

47. S. Ma, Z. Meng, R. Chen, K.-L. Guan, The hippo pathway: Biology and pathophysiology. *Annu. Rev. Biochem.* **88**, 577–604 (2019).

48. P.-J. Zhou, W. Xue, J. Peng, Y. Wang, L. Wei, Z. Yang, H. H. Zhu, Y.-X. Fang, W.-Q. Gao, Elevated expression of Par3 promotes prostate cancer metastasis by forming a Par3/aPKC/KIBRA complex and inactivating the hippo pathway. *J. Exp. Clin. Cancer Res.* **36**, 139 (2017).

49. R. Iwata, P. Casimir, E. Erkol, M. Boubakar, M. Planque, I. M. G. López, M. Ditkowska, V. Gaspariunaite, S. Beckers, D. Remans, K. Vints, A. Vandekeere, S. Poovathingal, M. Bird, I. Vlaeminck, E. Creemers, K. Wierda, N. Corthout, P. Vermeersch, S. Carpentier, K. Davie, M. Mazzone, N. V. Gounko, S. Aerts, B. Ghesquière, S.-M. Fendt, P. Vanderhaeghen, Mitochondria metabolism sets the species-specific tempo of neuronal development. *Science* **379**, eabn4705 (2023).

50. S. C. Fowler, L. J. Mosher, S. C. Godar, M. Bortolato, Assessment of gait and sensorimotor deficits in the D1CT-7 mouse model of tourette syndrome. *J. Neurosci. Methods* **292**, 37–44 (2017).

51. J.-C. Du, M.-H. Chang, C.-J. Yeh, M. T. Lee, H.-J. Lee, S.-H. Chuang, L.-C. Chiou, Pivotal role of Slitrk1 in adult striatal cholinergic neurons in mice: Implication in tourette syndrome. *Ann. Neurol.*, doi: 10.1002/ana.26805, (2023).

52. L. Song, S. Tang, X. Han, Z. Jiang, L. Dong, C. Liu, X. Liang, J. Dong, C. Qiu, Y. Wang, Y. Du, KIBRA controls exosome secretion via inhibiting the proteasomal degradation of Rab27a. *Nat. Commun.* **10**, 1639 (2019).

53. L. C. Farhat, E. Behling, A. Landeros-Weisenberger, J. L. S. Levine, P. M. F. de Barros, Z. Wang, M. H. Bloch, Comparative efficacy, tolerability, and acceptability of pharmacological interventions for the treatment of children, adolescents, and young adults with tourette's syndrome: A systematic review and network meta-analysis. *Lancet Child Adolesc. Health.* **7**, 112–126 (2023).

54. C. R. Gerfen, D. J. Surmeier, Modulation of striatal projection systems by dopamine. *Annu. Rev. Neurosci.* **34**, 441–466 (2011).

55. H. S. Singer, Tourette's syndrome: From behaviour to biology. *Lancet Neurol.* **4**, 149–159 (2005).

56. E. H. Ahn, S. S. Kang, Q. Qi, X. Liu, K. Ye, Netrin1 deficiency activates MST1 via UNC5B receptor, promoting dopaminergic apoptosis in parkinson's disease. *Proc. Natl. Acad. Sci. U.S.A.* **117**, 24503–24513 (2020).

57. C. Nasello, L. A. Poppi, J. Wu, T. F. Kowalski, J. K. Thackray, R. Wang, A. Persaud, M. Mahboob, S. Lin, R. Spaseska, C. K. Johnson, D. Gordon, F. Tissir, G. A. Heiman, J. A. Tischfield, M. Bocarsly, M. A. Tischfield, Human mutations in high-confidence tourette disorder genes affect sensorimotor behavior, reward learning, and striatal dopamine in mice. *Proc. Natl. Acad. Sci. U.S.A.* **121**, e2307156121 (2024).

58. R. Cadeddu, M. Van Zandt, L. S. Santovito, K. Odeh, C. J. Anderson, D. Flanagan, P. Nordkild, G. Pinna, C. Pittenger, M. Bortolato, Prefrontal allopregnanolone mediates the adverse effects of acute stress in a mouse model of tic pathophysiology. *Neuropsychopharmacology* **48**, 1288–1299 (2023).

59. Q. Gao, R. Tian, H. Han, J. Slone, C. Wang, X. Ke, T. Zhang, X. Li, Y. He, P. Liao, F. Wang, Y. Chen, S. Fu, K. Zhang, F. Zeng, Y. Yang, Z. Li, J. Tan, J. Li, Y. Lu, T. Huang, Z. Hu, Z. Zhang, PINK1-mediated Drp1S616 phosphorylation modulates synaptic development and plasticity via promoting mitochondrial fission. *Signal Transduct. Target. Ther.* **7**, 103 (2022).